Fuel 405 (2026) 136581

Contents lists available at ScienceDirect

Fuel

journal homepage: www.elsevier.com/locate/fuel

Full Length Article

A novel multi-generation system integrating thermophotovoltaic and SOFC system for power and green hydrogen with CO_2 liquefaction: A techno-economic and multi-objective optimization study

Shayan Rabet [a], Shayan Sharafi Laleh [a], Omid Habibi [a], Seyed Ali Sadri Jahanshahi [a], Mortaza Yari [a,*], Saeed Soltani [b,**]

[a] Faculty of Mechanical Engineering, University of Tabriz 16471 Tabriz, Iran
[b] Faculty of Engineering and Natural Sciences, Antalya Bilim University, 07190 Antalya, Turkey

ARTICLE INFO

Keywords:
Digestion
Solid oxide fuel cell (SOFC)
Thermophotovoltaic (TPV)
Vanadium Chloride (V-Cl)
Liquefaction

ABSTRACT

This study proposes a novel biomass-fueled multi-generation system that addresses key limitations in existing SOFC-based configurations, such as unutilized radiative heat and the lack of integrated CO_2 capture. The system integrates a digestion unit, solid oxide fuel cell (SOFC), thermophotovoltaic (TPV) unit, closed Brayton cycle, vanadium chloride hydrogen production cycle, and a CO_2 liquefaction module. A major innovation lies in recovering the SOFC's radiative waste heat via the TPV unit, significantly boosting total power output and improving overall sustainability. The system utilizes biogas and air in separate pathways for electrochemical and combustion processes, while waste heat is recovered to drive the Brayton cycle, support hydrogen production, and enable CO_2 liquefaction through LNG-based cooling. This integrated approach reduces fossil fuel dependency and greenhouse gas emissions. A comprehensive energy, exergy, techno-economic, and environmental analysis is performed, along with multi-objective optimization using the Grey Wolf Optimizer under two scenarios. Parametric studies identify the combustion chamber temperature as a key performance driver. The integration of TPV and cryogenic CO_2 capture improves energy utilization and environmental impact. The optimized system achieves a net power output of 2,798 kW, an exergy efficiency of 35.44 %, and a CO_2 emission index of 0.6353 kg/kWh. The system achieves a hydrogen production rate of 0.01285 kg/s, with payback periods ranging from under four to under seven years depending on electricity price and operational lifespan. These results confirm the proposed system's potential as a high-efficiency, low-emission solution for decentralized clean energy and fuel production.

1. Introduction

Growing fossil fuel use has caused environmental, health, and economic problems. Burning these fuels generates greenhouse gases, contributing to global warming and climate change. Fossil fuel extraction and use pollute air and water, degrade ecosystems, and affect human health through particulate matter and petrol emissions [1]. In light of these pressing issues, there is an increasing focus on green hydrogen as a sustainable energy solution, due to its capacity to reduce carbon emissions in industrial operations, stabilise renewable energy systems, and function as a zero-emission fuel for transportation and energy sectors [2,3]. Solid Oxide Fuel Cells (SOFCs) present a compelling option for high-efficiency power generation utilising hydrogen or biogas. Nonetheless, they face significant challenges, including elevated operating temperatures (800–1000 °C), material degradation, and ineffective radiative heat loss. These issues ultimately compromise their long-term performance and escalate maintenance expenses [4]. To address these challenges, Thermophotovoltaic (TPV) systems can be incorporated to harness the radiative heat from SOFCs and transform it into electricity, thus enhancing overall system efficiency without the need for extra fuel consumption [5]. Furthermore, the process of capturing and liquefying CO_2 significantly improves the environmental efficacy of the system while enabling the secure handling, storage, or repurposing of CO_2, in accordance with strategies for managing carbon within renewable energy frameworks [6].

* Corresponding author.
** Corresponding author.
E-mail addresses: myari@tabrizu.ac.ir (M. Yari), saeed.soltani@antalya.edu.tr (S. Soltani).

https://doi.org/10.1016/j.fuel.2025.136581
Received 12 June 2025; Received in revised form 11 August 2025; Accepted 19 August 2025
Available online 21 August 2025

Nomenclature

Symbols and abbreviations

A	Area [m^2]
Ab	After burner
AI	Annual Income [$]
bl	Plant lifetime [years]
CC	Combustion Chamber
CETD	Cold end temperature difference [K]
CEPCI	Cost index
CRF	Capital recovery factor
Comp	Compressor
CV	Control volume
D	Diameter [m]
D_{eff}	Effective diffusion of gas
EES	Engineering equation solver
E_0	Electromotive force
$\dot{E}x$	Exergy rate [kW]
$\dot{E}x_D$	Exergy destruction rate [kW]
FF	Fill factor
GT	Gas Turbine
HEX	Heat Exchanger
HP	High pressure
I_b	Blackbody radiative intensity [W/m^2]
IF	Inflation rate [%]
h	Specific enthalpy [kJ/kg]
i_r	Interest rate [%]
I	resultant current [A]
j	Current density [A/m^2]
J_{sc}	Short-circuit current [A/m^2]
K	Equilibrium constant
L	Thickness of a cell component [m]
LHV	Lower heating value [MJ/kg]
LP	Low pressure
$\dot{m}$	Mass flow rate [kg/s]
Mix	Mixer
MSW	Municipal Solid Waste
MOGWO	Multi-Objective Grey Wolf Optimization
N	Yearly operational duration [hours]
NPV	Net Present Value [M$]
P	Pressure [kPa]
PBP	Payback Period [year]
PEC	Purchase Equipment Cost [$]
PRC	Pressure ratio
$\dot{Q}$	Heat transfer rate [kW]
Ri	Real Inerest rate [%]
s	Specific entropy [kJ/(kg·K)]
S	surface area [m^2]
Sep	Seperator
SOFC	Solid oxide fuel cell
T	Temperature [K]
TPV	Thermophotovoltaic
Turb	Turbine
UF	Fuel utilization factor
VCl	Vanadium Chloride
V_{oc}	Open-circuit voltage [V]
$\dot{W}$	Power [kW]
$\dot{Z}$	Investment cost rate [$/year]

Greek symbols

ρ	Electrical resistivity [Ω • m]
η_{II}	Efficiency of exergy [%]
ε	Effectiveness factor [%]
ϕ_r	Maintenance factor
λ	Wavelength [μm]

Subscripts

0	Reference condition
a	Anode
act	Activation
c	Cathode
ch	Chemical
el	electrical
em	emitter
en	Energy
ex	Exergy
flt	filter
in	Inlet
imp	Impurities
is	Isentropic
net	Net
ohm	Ohmic
OM	Operation and maintain
out	Outlet
ph	Physical
Pump	Pump
q	Heat transfer rate
rad	radiation
ref	reflect
th	Thermal
tot	total
w	wall

Calise et al. [7] developed a dynamic simulation model for producing liquid biomethane from MSW through anaerobic digestion. The model incorporates gas upgrading, liquefaction, and renewable energy technologies like photovoltaic panels and solar heaters. It highlights energy conservation, carbon emission reduction, and economic benefits, improving port operations and efficiency in metropolitan regions.

Zare and Hasanzadeh [8] analyzed a novel Brayton-ORC combined cycle for solar power towers, using helium as the working fluid. Their study shows higher exergy efficiency (~30 %), outperforming Rankine and supercritical CO_2 cycles. They highlight the heliostat field's major exergy destruction and stress the need for efficient power cycles to improve CSP competitiveness.

Hai et al. [9] integrated a VCl thermochemical cycle with a nanoparticle-enhanced SPT for hydrogen and power cogeneration, supposing minimal pressure losses and adiabatic components. The system delivers 2420 kW of net power, 148 kg/h of hydrogen, an exergy efficiency of 21.1 %, and a 5.3 % increase in hydrogen production compared to conventional systems, while enhancing efficiency by 4–5 percent and decreasing costs by 3–4 percent. The system proposed by Safari et al. [10] could generate 885 kW of electricity and 23.42 kg/h of hydrogen by optimizing a VCl thermochemical cycle with algal biomass gasification, achieving an energy efficiency of 42.1 % and an exergy efficiency of 74.5 %. Optimization surpasses Cu-Cl systems by enhancing exergy efficiency to 60.45 %, decreasing costs to $6.36/GJ, and minimizing CO_2 emissions to 14.46 g/kWh at ideal gas conditions and complete gasification. To generate hydrogen, Balta et al. [11] analyzed the Cu-Cl, Mg-Cl, Fe-Cl, and VCl cycles. Demonstrating an impressive efficiency exceeding 40 % and an exergy efficiency of 77.28 %, VCl stands out against Fe-Cl, which lags at 18.5 %, while also being on par with Cu-Cl, which ranges from 15 % to 52 %, and Mg-Cl, which achieves

Table 1
A comprehensive overview of recent studies on systems, highlighting their limitations and deficits.

Reference	Limitations	Analyses Energy	Exergy	Techno-economic	Environment	Multi-objective optimization
Liao et al. [5]	No Digestion unit, No hydrogen production, No carbon dioxide liquefaction		×	×	×	×
Yari et al. [22]	No TPV unit, No carbon dioxide liquefaction				×	×
Ma et al. [18]	No TPV unit		×		×	×
Present work	–					

between 30 % and 65 %. Recent developments in LAES systems have demonstrated significant potential in multi-generation configurations. Ding et al. [12] proposed a solar-assisted LAES system capable of providing electricity, heating, cooling, hot water, and hydrogen. Their study highlighted a substantial increase in energy efficiency, achieving up to seventy-one percent efficiency, with economic advantages such as a net present value increase of over four hundred million USD. In a separate study, Ding et al. [13] presented the first emergy-based and sustainability LCA of a solar-aided LAES system. Results indicated a notable environmental sustainability index (ESI) of over 3.0 and optimal performance in solar-rich regions such as Dunhuang.

Zhang et al. [14] proposed a biomass-based CCHP system combining HT-PEMFC and SOFC technologies, achieving 49.48 % overall efficiency and 25.06 % energy efficiency. The system produces CO_2 emissions of 0.673 kg/kWh and has a production cost of $0.069/kWh. Increasing the SOFC operating temperature improved energy efficiency by 11.18 % and overall efficiency by 16.97 %. Saberi Mehr et al. [15] studied solar-powered proton exchange membrane electrolysis for hydrogen production in SOFC systems. Adding hydrogen to syngas increased product costs but reduced CO_2 emissions and improved heat and power efficiency by 3 %. Optimal values for temperature, current density, and hydrogen concentration were identified to enhance efficiency. Yang et al. [16] compared steam and dry reforming of various fuels to generate syngas in SOFC systems. Alcohols withstand carbon deposition better than hydrocarbons. SR-SOFC is more efficient with methane and methanol, whereas DR-SOFC wins with methane. High temperatures and fuel usage boost efficiency. The study also examines improving SOFC performance using a Kalina cycle, desalination unit, and electrolyser. Wen et al. [17] studied a solar-aided multi-generation system that generates electricity, heating, cooling, and hydrogen using a SOFC, thermal cooling system, and solar heat source. Analysis uses energy, exergy, economic, and exergoeconomic approaches. Solar integration boosts system efficiency, although the SOFC and cooling subsystems destroy the greatest exergy. With a 42.5 % total exergy efficiency, 0.0146 kg/s hydrogen generation, and 250 kW cooling capacity, the ideal configuration offers outstanding performance and environmental benefits. A complete techno-economic evaluation of small-scale biogas-fed SOFC systems incorporating unique biogas purification and CCS technologies is presented by Ma et al. [18]. A cryogenic purification and sodium carbonate loop (CBP-SOFC-SCL) system is compared to one with dual loops (SCL-SOFC-SCL) for purification and CCS. Their investigation found optimal operation points for the SCL-based design, which has a greater efficiency of 57.4 % and a lower LCOE of 0.150 €/kWh than the CBP setup's 53.6 % and 0.165 €/kWh. The new approach of combining sodium carbonate loop technology in fuel purification and CCS processes leads to greater thermal integration, reduced CO_2 emissions, and enhanced economic performance. Sensitivity analysis emphasise how recirculation ratio, reforming temperature, and stack replacement costs affect system viability. Li et al. [19] optimised two SOFC-GT-ST triple hybrid power systems with carbon capture and LNG cold energy recovery to improve thermal efficiency and minimise emissions. The combination of anode and rear combustion chamber exhaust gas recirculation, MDEA absorption and calcium looping carbon capture methods, and LNG cold energy cascade utilisation is novel in triple hybrid configurations. The study found optimal operating conditions using Aspen Plus thermodynamic modelling and optimisation. The system with MDEA capture has an electrical efficiency of 73.08 % and an exergy efficiency of 70.32 %, while LNG cold energy recovery adds 410.86 kW and 382.64 kW of electricity, proving integrated low-carbon strategies work.

After conducting a comprehensive literature review, this study proposes the integration of a thermophotovoltaic (TPV) unit with the SOFC to harness additional power from radiative heat losses, thereby improving the overall performance of the multi-generation system. Hybrid energy systems can enhance efficiency by repurposing TPV waste heat for electricity or heating. Using biomass-derived fuels and digesters instead of methane offers a sustainable alternative, reducing fossil fuel dependence and supporting a cleaner energy future. Shan et al. [20] integrated a TPV device with a steam Rankine cycle (SRC) to improve fuel conversion efficiency using a photo-thermal energy cascade. Their analysis showed an 11–13 % efficiency improvement over traditional SRC, with TPV reducing boiler exergy loss. Enhancing the emitter area and heat transfer, especially in silicon cells, boosted performance. The study highlights TPV's potential in improving SRC efficiency and suggests further exploration of advanced chemical energy conversion methods. Yang et al. [21] suggested a cogeneration system that recovers waste heat and improves efficiency using a DC-SOFC and TPVC. First-ever integration of a solid-state TPVC with a 2D tubular DC-SOFC model that rigorously accounts for electrochemical, mass, and heat transport phenomena. This arrangement lets the TPVC harvest radiative heat from the high-temperature DC-SOFC without mechanical components or fluids. The analysis numerically shows that the suggested system can produce 56.2 % greater power density than the stand-alone DC-SOFC and enhance efficiency. Results show that SOFC operating temperature, carbon layer-anode distance, and TPVC band-gap energy considerably affect performance and may be optimised to increase power production and system efficiency.

Table 1 presents a comprehensive overview of recent studies on SOFC-based systems, allowing for a comparison between the present work and both standalone SOFC systems and integrated multigeneration configurations. The table highlights key limitations, analytical gaps, and the absence of thorough multi-objective optimization in previous studies.

1.1. Principal developments and novelties

This study presents a novel multi-generation system that integrates biomass energy (from MSW) and TPV technology with advanced energy conversion and waste heat utilization strategies. The key innovation lies in harnessing the radiative waste energy from the biogas-fed Solid Oxide Fuel Cell (SOFC), which is captured by the TPV unit to enhance power generation compared to similar multi-generation systems. The other crucial contributions of this work include:

- Integration of biomass (MSW) in the digestion unit as a fuel for the SOFC, reducing reliance on methane and improving sustainability.
- Absence of comprehensive multi-generation analyses in previous SOFC and TPV studies, as shown in Table 1.

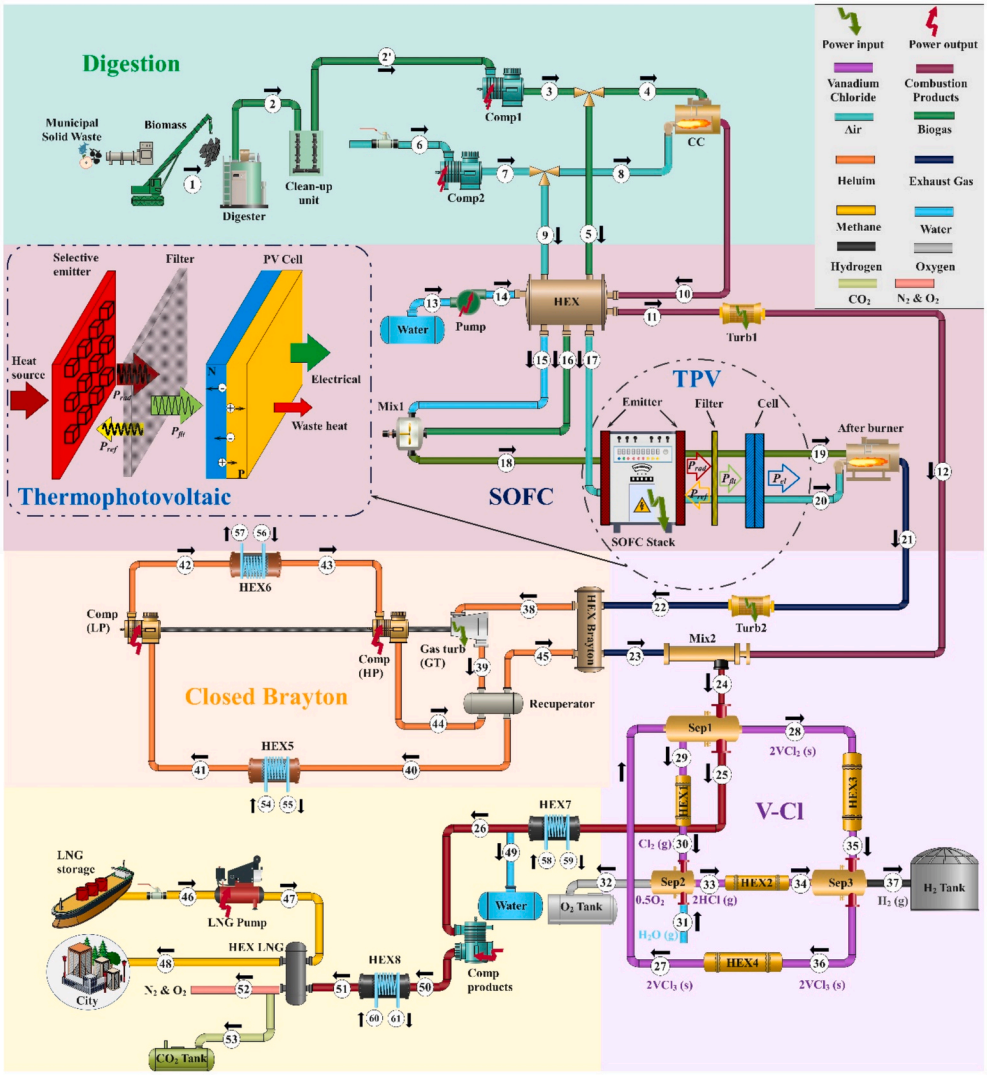

Fig. 1. Schematic of the suggested multi-generation framework.

- Implementation of the Vanadium Chloride (VCl) cycle for hydrogen production using waste heat, providing efficient hydrogen generation without additional energy input.
- Use of LNG for cooling and CO_2 liquefaction, reducing emissions and improving environmental performance.
- Comprehensive energy, exergy, techno-economic, and environmental analyses, including the evaluation of the system's economic feasibility through net present value (NPV) under different electricity price scenarios.
- Extensive parametric analysis of system performance, covering efficiency, power output, hydrogen production, and emission index, demonstrating superior thermodynamic and environmental performance without direct CO_2 emissions.
- Optimization using Multi-Objective Grey Wolf Optimizer (MOGWO) in two scenarios to enhance efficiency and economic viability.
- Introduction of a helium-based closed Brayton cycle for waste heat recovery, replacing conventional CO_2 or ORC cycles, which improves overall thermal management.
- Practical application for small villages, using MSW to generate electricity for the local community, and selling liquefied CO_2 and hydrogen to promote economic development in remote areas with sufficient biomass resources.

These innovations collectively contribute to a high-efficiency, low-emission multi-generation system, advancing clean energy production, waste heat recovery, emission reduction, and economic sustainability in rural areas.

1.1.1. *System flexibility and challenges*

Modular components can adapt to energy and resource demands, making the system suitable for small villages. The digesting unit and SOFC dimensions depend on biomass availability, whereas the TPV unit responds to waste heat. Reducing scale may reduce biogas output, requiring feedstock management or digestion length changes. At lower scales, SOFC and Brayton cycle waste heat recovery may be less efficient. Smaller systems may require more maintenance due to component thermal inertia and longer initiation and cessation times. Overly lowering scale can cause challenges in biogas production or CO_2 liquefaction.

1.2. *Structure of paper*

The organization of the document is presented as follows:

Section 2: Provides a comprehensive analysis of the proposed multi-generation system, detailing its components and the operational framework in a structured manner.

Section 3: Explores the intricate mathematical modeling of the system, meticulously divided into several segments:

- Assessments of Mass and Energy: Emphasizes the essential performance indicators.
- Subsystem Analysis: Investigates the intricacies of the digestion unit, SOFC, TPV, and the vanadium chloride cycle (VCl).
- Exergy Efficiency: Evaluates the system's performance in accordance with the principles of the second law of thermodynamics.
- Assessment of Economic Factors: Connects the system's effectiveness with its financial dimensions.
- Multi-Objective Optimization with Grey Wolf Algorithm: Outlines the strategic process and its aims.

Section 4: Affirms the model to ensure the precision and reliability of the evaluations.

Section 5: Analyzes the outcomes and links the findings to the overarching efficacy of the system.

Section 6: Concludes with an integration of the principal findings and wider effects of the study.

2. Description of the suggested system

The proposed system is illustrated in Fig. 1, showcasing the integration of various components designed to optimize energy efficiency and output. The system includes the following elements:

- **Digestion Unit**: This unit uses biomass to produce biogas, which is then utilized to generate power.
- **SOFC Unit**: The SOFC unit uses a mixture of biogas from the digestion unit, along with air and water, to produce electricity.
- **Thermophotovoltaic Unit**: The radiation from the SOFC unit, which is typically lost as heat in conventional systems, is redirected to the TPV unit, where it is converted into additional power.
- **Closed Brayton Cycle**: This unit helps lower the temperature of the system and utilizes the waste heat from the SOFC cycle to enhance performance.
- **VCl Unit**: This unit uses waste heat from both the digestion and SOFC units to produce hydrogen, contributing to overall system efficiency.
- **Liquefaction Unit**: This unit uses LNG to cool the products and separate CO_2, converting it into a liquid form for potential storage or further use.

The thermodynamic coupling between these components facilitates an efficient energy exchange across the system. The heat and exergy flows are as follows:

2.1. Digestion unit

Biomass is fed into the digester at state 1, where it undergoes moisture reduction, producing biogas at state 2. The biogas is then compressed in Compressor 1, increasing its pressure at state 3. Simultaneously, ambient air enters Compressor 2 at state 6, undergoes compression, and exits at state 7. A portion of the compressed biogas at state 3 and compressed air at state 7 enter the combustion chamber (CC) at states 4 and 8, respectively. The combustion process generates high-temperature exhaust gases, which exit at state 10 and pass through a heat exchanger (HEX) to preheat the air, water, and biogas before entering the SOFC unit. The partially cooled exhaust gases exit the HEX at state 11 and then expand in Turbine 1, generating electricity before leaving at state 12.

2.2. Solid oxide fuel cell (SOFC) unit

Water enters at state 13 and is pumped to a higher pressure at state 14. It is then preheated in the HEX before entering the SOFC. Heated biogas and water at states 15 and 16 are mixed and supplied to the SOFC anode at state 18. Simultaneously, preheated air at state 17 enters the SOFC cathode, enabling the electrochemical reaction that generates power. The unreacted fuel and steam exit the anode at state 19, while the depleted air exits the cathode at state 20. These streams are directed into an afterburner, where additional combustion occurs. The exhaust gases from the afterburner exit at state 21 and expand in Turbine 2, producing additional power before being discharged at state 22.

2.3. Thermophotovoltaic unit

The waste heat radiated from the SOFC is captured in the TPV unit. The thermal radiation passes through a filter, where part of it is reflected while the remaining portion is transmitted to photovoltaic cells to generate power. Any residual heat is considered waste, but its contribution is minimized by the efficiency of the TPV unit in converting the SOFC's waste heat.

2.4. Closed Brayton cycle

The closed Brayton cycle (CBC) utilizes helium as a working fluid. The helium absorbs waste heat from the SOFC in the Brayton heat exchanger and enters the gas turbine (GT), generating power before exiting at state 39. The helium then passes through a recuperator, where it preheats the incoming stream for improved efficiency before exiting at state 40. The helium is further cooled at state 41 in HEX5 to reduce the power consumption of the low-pressure compressor (LP). After compression at LP, the helium exits at state 42 and enters HEX6, where it is further heated before being compressed at high pressure (HP) at state 44. The heated helium then passes through the recuperator again before re-entering the Brayton heat exchanger, completing the cycle.

2.5. Vanadium chloride (VCl)

Exhaust gases at state 23 and combustion products at state 12 mix in Mixer 2 and exit at state 24. The waste heat is used in the vanadium-chloride system before the gas exits at state 25. In this cycle, 2 mol of VCl_3 in solid form enter Separator 1, where they dissociate into 2 mol of VCl_2 in solid form at state 28 and 1 mol of Cl_2 gas at state 29. The separated VCl_2 enters HEX3 and exits at state 35, while the Cl_2 gas enters HEX1 and exits at state 30. Water enters at state 31 and reacts with Cl_2 in Separator 2, producing 2 mol of gaseous HCl at state 33, which then passes through HEX2 and exits at state 34. The chemical reaction in Separator 3 produces hydrogen at state 37, while 2 mol of VCl_3 enter HEX4 at state 36 and exit at state 27, completing the cycle. Oxygen is released from Separator 2 at state 32.

2.6. Liquefaction unit

The mixed gas stream enters HEX7, where it is cooled, allowing water to be separated from the stream at state 49. The remaining gas exits at state 26 and is compressed in a product compressor, increasing its pressure at state 50 before being further cooled at state 51. LNG in liquid form enters at state 46, is pumped at state 47, and flows through HEX LNG to provide cooling. This process enables the liquefaction of CO_2, which exits at state 53 and is then stored or utilized at state 48. The remaining products exit at state 52.

To optimize CO_2 liquefaction, the exhaust gases are first cooled in HEX7 to reach the condensation temperature of water. Afterward, the remaining gases, primarily CO_2, N_2, and oxygen, are compressed. To condense CO_2 efficiently, the system ensures that the gas reaches a high pressure, thereby minimizing the mass flow rate of LNG required for liquefaction. After reaching the high pressure, the gas enters HEX8, where it is cooled by water. The cooling is then completed by LNG in HEX LNG. Utilizing multiple compressors for the exhaust gas increases condensation temperature, which decreases exergy destruction and total expenses.

In the proposed system, heat and exergy flow through the components in a cascading manner, where waste heat from one component is

Table 2
Assumptions for the digestion subsystem.

Parameter	Value	Unit	Reference
Reference pressure, P_0	101.3	*kPa*	[12]
Reference temperature, T_0	298	*K*	[13]
Pressure ratio of compressors, PR_{comp}	16	–	[29]
Pressure ratio of pumps, PR_{pump}	16	–	[29]
Isentropic efficiency of turbines, $\eta_{is,Tur}$	85	%	[24]
Isentropic efficiency of compressors, $\eta_{is,Comp}$	85	%	[24]
Isentropic efficiency of pumps, $\eta_{is,Pump}$	85	%	[24]
Digestion temperature, T_2	328	*K*	[24]
Combustion temperature, T_{10}	1500	*K*	[24,31]
Fuel ratio of biogass for CC, FR_4	0.63	–	–

recovered and used by another. Specifically:

- The SOFC unit generates high-temperature exhaust gases, part of which is redirected to the TPV unit for power generation.
- Exhaust gases from the digestion unit and SOFC are combined and used to generate hydrogen in the VCl unit, contributing to system efficiency by converting waste heat into chemical energy (hydrogen).
- The CBC and Liquefaction Unit recover and further utilize the waste heat, ensuring that exergy is maximized across the system.

3. Mathematical modeling

The examination was carried out through the development of a simulation utilizing Engineering Equation Solver (EES) software. Furthermore, the process of multi-objective optimization is executed utilizing MATLAB software. The examination encompasses the preservation of mass and energy alongside exergy and financial assessments, all articulated through the foundational tenets of thermodynamics.

The fundamental assumptions underlying the modeling are in the following sections:

- The system operates under steady-state condition [23].
- The implications of alterations in kinetic and potential energies are ignored [23].
- A reduction in pressure was observed within the combustion chamber and after burner, registering at a level of 3 % at their outlets. The pressure reductions in the connecting pipes have been disregarded [24].
- The air entering the digester complex from the second compressor is comprised of 20.59 % oxygen, 77.48 % nitrogen, 0.30 % carbon dioxide and 1.9 % water [25].
- The gases within the multi-generation system maintain to the principles of ideal gas behavior [24].
- The combustion chamber, the afterburner, and all the heat exchangers are subject to thermal insulation measures [24].
- The most significant heat transfer within the vanadium chloride cycle occurs during sep 1 (step 1), with the heat transfer rates of subsequent seperators (steps) and heat exchangers being comparatively lower. Consequently, the heat transfer of the heat exchangers is solely factored into the calculation of exergy efficiency [11].

3.1. Thermodynamic analysis

The concept of energy conservation, rooted in the law of thermodynamics, is employed to assess the conditions of each flow at the inlet and outlet of the control volume, as articulated in the equations relating to mass and energy balance [26]:

$$\sum_{in}\dot{m} = \sum_{out}\dot{m} \tag{1}$$

$$\dot{Q} + \sum_{in}\dot{m}h = \sum_{out}\dot{m}h + \dot{W} \tag{2}$$

The exergy balance equation for a control volume functioning under steady state is expressed as follows [27]:

$$\sum_{Inlets}\dot{E}_i + \sum\dot{Q}_j\left(1-\frac{T_0}{T_j}\right) = \sum_{Outlets}\dot{E}_e + \dot{W}_{cv} + \dot{I}_{cv} \tag{3}$$

The total exergy of a stream, $\dot{E}$, is the sum of the physical and chemical exergies of the stream:

$$\dot{E} = \dot{E}_{ph} + \dot{E}_{ch} \tag{4}$$

The calculation of the physical exergy of a stream is conducted by disregarding both kinetic and potential energies, as outlined in the following equation [28]:

$$\dot{E}_{th} = \sum\dot{m}_i[(h_i - h_0) - T_0(s_i - s_0)] \tag{5}$$

The calculation of the chemical exergy of a mixture of ideal gases is conducted as follows [27]:

$$\dot{E}_{ch} = \dot{n}\left(\sum y_i\bar{e}_i^{ch,0} + \bar{R}T_0\sum y_i ln(y_i)\right) \tag{6}$$

where, y_i represents the mole fraction of each species within the mixture, and $\bar{e}_i^{ch,0}$ denotes the standard chemical exergy associated with the species.

The energy and exergy balances of the system components are provided in Table S1 of the supplementary file for further reference [27].

Exergy efficiency is fundamentally measured as the ratio of the exergy of the output or product to the exergy of the total fuel input [28]:

$$\varepsilon_i = \frac{\dot{E}_P}{\dot{E}_F} = 1 - \frac{\dot{E}_D + \dot{E}_L}{\dot{E}_F} \tag{7}$$

3.2. Digestion units

A thermophilic anaerobic digester, operating at a temperature of 328 K, was employed for the digestion process in this study, with a retention time of 14 days. To ensure optimal microbial activity, any fluctuations in temperature during the digestion process are considered negligible. The analysis of biogas production is exclusively derived from the organic (ash-free) component of Municipal Solid Waste (MSW), following the methodology established by Zhang et al. [29]. The widely recognized equation for the digestion of biomass is presented as follows [30]:

$$(0,95\times 0,7)\times n_{MSW}C_{100}H_{196}O_{38} + wH_2O \rightarrow n_1CO_2 + n_2CH_4 \tag{8}$$

In this study, it is suggested that approximately 95 % of the biomass consists of volatile compounds, with nearly 70 % of these being decomposable and convertible into biogas through the activity of anaerobic bacteria. The remaining fraction is discharged from the digester as liquid manure. Given the negligible production of other gases during the anaerobic digestion process, their impact on system behavior has been disregarded. Furthermore, biogas cleaning systems—such as activated carbon filters and iron oxide beds—require minimal energy input and entail negligible operational costs. As a result, their influence on overall system performance is insignificant. Therefore, the biogas is assumed to be sufficiently purified before entering the SOFC, without compromising the accuracy of the energy and exergy analyses [22,29].

The moisture content of the MSW is calculated using the following formula [30]:

$$MC_{MSW} = \frac{w\times 18}{1+(w\times 18)}\times 100 \tag{9}$$

where w represents the water content in the MSW.

The heat required to process the feedstock is given by [29]:

Table 3
The enthalpy of formation, reference entropy, and Shomate coefficient data for the compounds in the VCl cycle [10,11].

Compounds	$\bar{h}_f^0\left(\frac{kJ}{mole}\right)$	$\bar{s}_0\left(\frac{J}{mole,K}\right)$	A	B	C	D	E	F	G	H
$H_2O_{(g)}$	−241.83	188.84	−203.6	1523.29	−3196.4	2474.45	3.855	−265.55	−488.72	−285.83
$Cl_{2(g)}$	0	223.08	33.051	12.23	−12.065	4.385	−0.159	−10.834	259.03	0
$O_{2(g)}$	0	205.15	31.322	−20.235	57.866	−36.5	−0.007	−8.903	246.8	0
$H_{2(g)}$	0	130.68	33.066	−11.363	11.432	−2.772	−0.0158	−9.981	172.7	0
$HCl_{(g)}$	−92.31	186.9	32.124	−13.458	19.868	−6.854	−0.049	−101.62	228.68	−92.312

Table 4
Assumptions for the closed-Brayton subsystem.

Parameter	Value	Unit	Reference
Effectiveness of HEX5, HEX6, HEX7 and HEX8, ϵ_{HEX}	90	%	[8]
Cold end temperature difference of HEX Brayton, $CETD_{HEX,BR}$	200	*K*	–
Cold end temperature difference of Sep1 in V-Cl, $CETD_{Sep1,VCl}$	125	*K*	[8]
Inlet pressure to heluim turbine, P_{38}	7320	*kPa*	[8]
Helium turbine polytropic efficiency, $\eta_{He,Turbine}$	0.932–0.0117ln (PR_T)	–	[8]
Helium compressor polytropic efficiency, $\eta_{He,Compressor}$	0.916–0.0175ln (PR_C)	–	[8]
LP Compressor inlet pressure, P_{41}	2500	*kPa*	[8]
Helium pressure loss in recupartor (HP flow), $\Delta P_{HP,Recupartor}$	80	*kPa*	[8]
Helium pressure loss in recupartor (LP flow), $\Delta P_{LP,Recupartor}$	50	*kPa*	[8]
Helium pressure loss in other HEX6, ΔP_{HEX6}	80	*kPa*	[8]

$$\dot{Q}_{feedstock} = \dot{m}_{MSW} \times C_{MSW} \times (T_2 - T_0) \tag{10}$$

Here, C_{MSW} is the specific heat capacity.

Table 2 summarizes the assumptions applied in modeling the digestion subsystem.

3.3. Vanadium-chloride cycle

The procedures of the VCl thermochemical cycle and the corresponding reactions are outlined as follows [32]:

$$2VCl_{3(s)} \rightarrow 2VCl_{2(s)} + Cl_{2(g)}\, Temp = 798K (\text{Step } 1) \tag{11}$$

$$Cl_{2(g)} + H_2O_{(g)} \rightarrow 2HCl_{(g)} + \frac{1}{2}O_{2(g)}\, Temp = 373K (\text{Step } 2) \tag{12}$$

$$2VCl_{2(s)} + 2HCl_{(g)} \rightarrow 2VCl_{3(s)} + H_{2(g)}\, Temp = 573K (\text{Step } 3) \tag{13}$$

The energy and exergy rates at each stage are meticulously calculated to scrutinize the cycle and evaluate its overall efficiency. It is crucial to recognize that the assumptions employed in this analysis are consistent with those outlined in reference [11]. In a typical steady-state, steady-flow scenario, the equations governing mass, energy, and exergy balance are employed to determine the input heat, the rate of exergy destruction, and the efficiency of energy utilization [10].

$$\bar{h}(T) - \bar{h}_0 = A(T) + B\left(\frac{T^2}{2}\right) + C\left(\frac{T^3}{3}\right) + D\left(\frac{T^4}{4}\right) - \frac{E}{T} + F - H\left(\frac{kJ}{mole}\right) \tag{14}$$

$$\bar{s}(T) = A[\ln(T)] + B(T) + C\left(\frac{T^2}{2}\right) + D\left(\frac{T^3}{3}\right) - \frac{E}{(2T^2)} + G\left(\frac{J}{mole,K}\right) \tag{15}$$

$$C_P(T) = A + B(T) + C(T^2) + D(T^3) + \frac{E}{T^2}\left(\frac{J}{mole,K}\right) \tag{16}$$

The values of the constants from the aforementioned equations are presented in Table 3.

The Table 3 presented outlines the constants for hydrogen and chlorine gases within the temperature range of 298–1000 K, as well as for hydrogen chloride gas from 298 to 1200 K. In order to determine the enthalpy and specific heat capacity of VCl_2 and VCl_3 as they relate to temperature, we will utilize the data presented in reference [11], which outlines the correlation between these properties and temperature fluctuations.

For VCl_2:

$$\bar{h}(T) - \bar{h}_0 = (17,25)T + (1,36 \times 10^{-3})T^2 + (0,71 \times 10^5)T^{-1} - 5502 \tag{17}$$

$$C_P(T) = (17,25) + (2,72 \times 10^{-3})T - (0,71 \times 10^5)T^2 \tag{18}$$

For VCl_3:

$$\bar{h}(T) - \bar{h}_0 = (22,99)T + (1,96 \times 10^{-3})T^2 + (1,68 \times 10^5)T^{-1} - 7592 \tag{19}$$

$$C_P(T) = (22,99) + (3,92 \times 10^{-3})T - (1,68 \times 10^5)T^2 \tag{20}$$

The equations hold relevance for VCl_2 across the temperature spectrum of 298–1200 K, and for VCl_3 within the range of 298–900 K. It is crucial to recognize that the enthalpy is expressed in units of cal/mole, whereas the specific heat is represented in cal/mole.K. The enthalpy of formation values for VCl_2 and VCl_3 stand at −452.17 kJ/mole and −581.13 kJ/mole, respectively. The entropy values for VCl_2 and VCl_3 stand at 0.0493 kJ/mole.K and 0.06462 kJ/mole.K, respectively [11].

Furthermore, the established chemical exergy values for the reactants and products are presented in [33].

Table 4 summarizes the assumptions applied in modeling the closed-Brayton cycle subsystem.

3.4. Solid oxide fuel cell unit

The process by which the reaction mechanism operates within the SOFC stack under the application of internal reforming can be delineated as follows [34]:

$$a_r \rightarrow [CH_4 + H_2O \leftrightarrow CO + 3H_2] (\text{Reforming}) \tag{21}$$

$$b_r \rightarrow [CO + H_2O \leftrightarrow CO_2 + H_2] (\text{Shifting}) \tag{22}$$

$$c_r \rightarrow \left[H_2 + \frac{1}{2}O_2 \leftrightarrow H_2O\right] (\text{Overall electrochemical reaction}) \tag{23}$$

The rates of molar conversion for equations (21)-(23) are identified as a_r, b_r, and c_r, respectively.

The hydrogen utilized in the fuel cell can be expressed in the format that follows [34]:

$$c_r = UF(3a_r + b_r) \tag{24}$$

UF denotes the variable that signifies the effectiveness of fuel utilization within the system.

The air utilization ratio, reflecting the share of air effectively engaged in reactions while disregarding non-reactive applications, can

Table 5
Equilibrium constants for reactions [35].

	Shift	Reforming
A	5.47302×10^{-11}	-2.63122×10^{-11}
B	-2.57478×10^{-7}	1.24067×10^{-7}
C	4.63741×10^{-7}	-2.25233×10^{-7}
D	-3.91501×10^{-1}	1.95027×10^{-1}
E	11.2096	−66.1396

be calculated as [34]:

$$U_O = \frac{c_r}{2\dot{n}_{O_2,3}} \tag{25}$$

The flow rate of substances measured in moles of gases is determined through the application of mass balances, as outlined in equations (21)-(23) (refer to Table 5). The variable $\dot{n}$ signifies the rate at which molar flow occurs. The molar concentrations of the elements are presented in Table 5, with y representing the concentration of each component within the flow [34].

The subsequent statement delineates the expressions for the equilibrium constants related to the shift and reforming processes, respectively [34]:

$$K_r = \frac{y_{CO} \times y^3{}_{H_2}}{y_{CH_4} \times y^3{}_{H_2O}} \left(\frac{P}{P_{ref}}\right)^2 = \frac{\dot{n}_{CO} \times \dot{n}^3{}_{H_2}}{\dot{n}_{CH_4} \times \dot{n}^3{}_{H_2O}} \left(\frac{P}{\dot{n}_{tot} \times P_{ref}}\right)^2 \tag{26}$$

$$K_s = \frac{y_{CO_2} \times y_{H_2}}{y_{CO} \times y_{H_2O}} = \frac{\dot{n}_{CO_2} \times \dot{n}_{H_2}}{\dot{n}_{CO} \times \dot{n}_{H_2O}} \tag{27}$$

The equilibrium constants K_r and K_s exhibit a direct correlation with temperature [35].

$$logK = AT^4 + BT^3 + CT^2 + DT + E \tag{28}$$

The values for A, B, C, D, and E can be found in Table 5.

The disparity in thermodynamic potentials arising from the electrode reactions dictates the reversible cell voltage, commonly referred to as the electromotive force (emf). The electromotive force is precisely articulated through the Nernst equation [34]:

$$E_0 = -\frac{\Delta\bar{g}^0}{2F} + \frac{\bar{R}.T_{FC,e}}{2F} ln\left(\left(\frac{y_{H_2} \times \sqrt{y_{O_2}}}{y_{H_2O}}\right) \times \sqrt{\frac{P}{P_{ref}}}\right) \tag{29}$$

where:

$$\Delta\bar{g}^0 = \bar{g}^0_{H_2O} - \bar{g}^0_{H_2} - \frac{1}{2}\bar{g}^0_{O_2} \tag{30}$$

$$\bar{g}^0 = \bar{h} - T_{FC,e}.\bar{s}^0 \tag{31}$$

In this context, $\Delta\bar{g}^0$ signifies the Gibbs free energy, $\bar{R}$ denotes the universal gas constant, $T_{FC,e}$ pertains to the temperature at the exit of the SOFC, and F stands for the Faraday constant. Moreover, $\bar{h}$ signifies the enthalpy per unit of molar flow rate, whereas $\bar{s}^0$ indicates the standard entropy per unit of molar flow rate.

The Nernst voltage signifies the peak voltage attainable in a fuel cell under conditions where electrical current is absent. The cell voltage diminishes from its open-circuit voltage as a result of polarization losses, which can be articulated mathematically as [34]:

$$V_C = E_0 - (\eta_{ohm} + \eta_{act} + \eta_{conc}) \tag{32}$$

The variables η_{ohm}, η_{act}, and η_{conc} signify the activation polarization, ohmic polarization, and concentration polarization, respectively.

Ohmic polarization stands as a pivotal element across all fuel cell varieties, as articulated by Bossel and Dubal [36] in the following manner [34]:

$$\eta_{ohm} = (R_C + \rho_C L_C + \rho_a L_a + \rho_e L_e + \rho_{int} L_{int}).j \tag{33}$$

where:

$$\rho_e = \left(3.34 \times 10^4 exp\left(-10300/T_{FC,e}\right)\right)^{-1} \tag{34}$$

$$\rho_a = \left(95 \times 10^6/T_{FC,e} exp\left(-1150/T_{FC,e}\right)\right)^{-1} \tag{35}$$

$$\rho_c = \left(42 \times 10^6/T_{FC,e} exp\left(-1200/T_{FC,e}\right)\right)^{-1} \tag{36}$$

$$\rho_{int} = \left(9.3 \times 10^6/T_{FC,e} exp\left(-1100/T_{FC,e}\right)\right)^{-1} \tag{37}$$

In this structure, R_C signifies the resistivity of the contact, ρ indicates the electrical resistivity of the cell components, L denotes the thickness of a cell component, and j represents the current density. The subscripts *ohm*, *c*, *a*, *e* and int denote the respective terms ohmic, cathode, anode, electrolyte, and interconnect.

Activation polarization emerges when the processes occurring at the electrode–electrolyte interface surpass their inherent energy barriers. Kim et al. [37] articulates the detriments associated with activation polarization in the following manner:

$$\eta_{act} = \eta_{act,a} + \eta_{act,c} \tag{38}$$

where:

$$\eta_{act,a} = \frac{\bar{R}.T_{FC,e}}{F}.\left(sinh^{-1}\left(\frac{j}{2j_{0a}}\right)\right) \tag{39}$$

$$\eta_{act,c} = \frac{\bar{R}.T_{FC,e}}{F}.\left(sinh^{-1}\left(\frac{j}{2j_{0c}}\right)\right) \tag{40}$$

In this context, j_{0a} represents the exchange current density of the anode, while j_{0c} represents the exchange current density of the cathode.

As electric current flows, disparities in concentration gradients emerge, leading to fluctuations in species concentrations at the boundaries of the three phases. The disparities in concentration lead to notable losses, especially when the fuel cell stack is supplied with impure fuel or oxidant gases. Chan et al. [38] articulate the concept of concentration polarization as follows:

$$\eta_{conc} = \eta_{conc,a} + \eta_{conc,c} \tag{41}$$

where:

$$\eta_{conc,a} = \frac{\bar{R}.T_{FC,e}}{2F}.\left(ln\left(1 + \frac{P_{H_2}.j}{P_{H_2O}.j_{as}}\right) - ln\left(1 - \frac{j}{j_{as}}\right)\right) \tag{42}$$

$$\eta_{conc,c} = -\left(\frac{\bar{R}.T_{FC,e}}{F}.ln\left(1 - \frac{j}{j_{cs}}\right)\right) \tag{43}$$

$$j_{as} = \frac{2F.P_{H_2}.D_{aeff}}{\bar{R}.T_{FC,e}.L_a} \tag{44}$$

$$j_{cs} = \frac{4F.P_{O_2}.D_{ceff}}{\left(\left(\frac{P_4 - P_{O_2,4}}{P_4}\right)\bar{R}.T_{FC,e}.L_c\right)} \tag{45}$$

In this framework, D_{aeff} signifies the effective diffusion of gas through the anode, whereas D_{ceff} denotes the effective diffusion of gas across the positive electrode (cathode).

The output efficiency produced by the solid oxide fuel cell (SOFC) stack can be assessed in the following manner:

$$\dot{W}_{FC,stack} = N_{FC}.I.V_c \tag{46}$$

N_{FC} represents the quantity of cells, while I denotes the resultant current. The resulting current I and current density j can be expressed as:

Table 6
Assumptions for the SOFC subsystem.

Parameter	Value	Unit	Reference
Input temperature of SOFC, T_{15} , T_{16} , T_{17}	1000	K	[34]
Output temperature of SOFC, T_{19} , T_{20}	1100	K	[34]
Current density, j	8000	A/m^2	[34]
Fuel utilization fastor, UF	0.8	–	[34]
Layer thickness of anode, S_{SOFC}	0.04	mm	[39]
Thermal conductivity of SOFC, K_{SOFC}	2	W/mK	[39]
Stack pressure drop	2	%	[22]

$$I = j.A_a \tag{47}$$

$$j = \frac{2FC_r}{N_{FC}.A_a} \tag{48}$$

In this context, A_a represents the active surface area, while C_r refers to the rate of molar conversion related to the total electrochemical reaction mechanism $H_2 + \frac{1}{2}O_2 \rightarrow H_2O$. Table 6 summarizes the assumptions applied in modeling the SOFC subsystem.

To describe heat transfer from the stack to the TPV, a simplification can be made by assuming an average temperature for both the entire outer surface of the stack and the entire inner surface. Since different heat transfer mechanisms require separate conservation of the two heat fluxes, two distinct averages are necessary. Consequently, for a generic inner surface, the boundary condition can be expressed as follows [39]:

$$\dot{Q}_{rad,SOFC} = \sigma\varepsilon_{SOFC}A_{SOFC}\left({T_{mean}}^4 - {T_0}^4\right) + \frac{k_{SOFC}}{S_{SOFC}}A_{SOFC}(T_{mean} - T_0) \tag{49}$$

where, $\sigma = 5.67 \times 10^{-8}(\frac{W}{m^2K^4})$ is the Stephan-Boltzmann constant, k_{SOFC} is the thermal conductivity and assumed $2(\frac{W}{mK})$, S_{SOFC} is the layer thickness of anode and assumed 0.04 (mm), T_0 is the ambient temperature, A_{SOFC} is the area of SOFC, and T_{mean} is the mean temperature of SOFC that calculated by the mean temperature of input and output of SOFC unit [39].

While the use of biogas in SOFCs introduces the risk of degradation, particularly through carbon deposition (coking) at the anode, its renewable nature continues to make it an attractive fuel for sustainable energy systems. As highlighted in recent reviews, SOFCs face significant durability and stability challenges that hinder their commercial viability, yet most current research still prioritizes power density improvements over long-term performance [40]. The electrodes—especially the anode exposed to carbon-containing fuels like biogas—are most susceptible to degradation due to poisoning (e.g., coking) and structural deterioration under chemical and thermal stresses. However, ongoing advancements in degradation mitigation techniques, including dopant addition, microstructural optimization, interface engineering, and protective coatings, are showing promise in extending SOFC lifespans. Despite these degradation concerns, the ability of biogas to reduce net carbon emissions and support circular energy systems provides a strong rationale for its continued investigation as an SOFC fuel.

To minimize the risk of carbon deposition in the present system, operation is maintained at a steam-to-carbon (S/C) ratio of 2.5 and a reforming temperature of 1100 K. According to the thermodynamic analysis shown in Fig. 2, adapted from [41], this operating point lies within the carbon-free zone, effectively preventing solid carbon formation.

Operating under these conditions promotes long-term catalyst stability and system integrity, without requiring additional protective mechanisms. Although a higher S/C ratio leads to increased water usage and a moderate rise in heat demand, this trade-off is considered acceptable in light of the enhanced reliability and the effective prevention of carbon-related degradation.

3.5. Thermophotovoltaic unit

The TPV system is assumed to recover radiative and convective heat from the inner wall of the insulated SOFC enclosure, where high temperatures are maintained during operation. This approach follows previous modeling studies, such as Yang et al. [21], which place the TPV receiver near the SOFC housing, and others by Liao et al. [5,42] and Dong et al. [43], which adopt similar assumptions for SOFC–TPV integration. Although no experimental system has yet demonstrated this configuration, it remains a commonly accepted basis for theoretical analysis.

The outer side of SOFC stack walls are covered by the emitters so that they can emit the wasted energy to the ambient. The thermal radiation

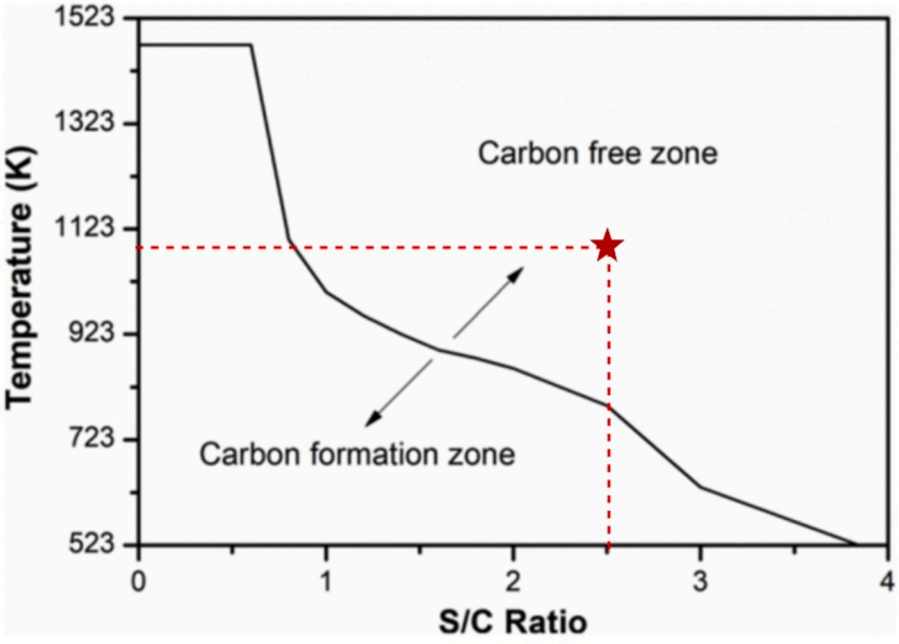

Fig. 2. For biogas compositions ranging from 45/55 to 80/20, carbon formation and carbon-free zones at different temperatures and S/C [41].

Table 7
Coefficients for EQE fitting formula [45].

	λ	A	B	C	D	E	F
Silicon	$298 < \lambda < 652nm$	1.972520059E + 3	−1.707929083E + 1	5.464737856E-2	−7.470290742E-5	3.726888675E-8	0
	$652 < \lambda < 1178nm$	−2.713351231E + 4	1.609912944E + 2	−3.768227025E-1	4.362154125E-4	−2.495276528E-7	5.635111095E-11

Table 8
Assumptions for the TPV subsystem.

Parameter	Value	Unit	Reference
Energy band gap, E_g	1.1	eV	[45]
Surface area of emitter, A	0.045	m^2	[45]
Radiative emissivity of the emitter, ε_{em}	0.9	–	[45]
Diode ideality factor, Γ	1	–	[45]
Number of cells in TPV, Num_{cell}	185	–	–
Correction factor, β	0.96	–	[45]

energy which is emitted can be calculated by Eq. (49).

I_b is the blackbody radiative intensity which is defined by the relation below [44]:

$$I_b = \frac{2hc^2}{\lambda^5}\frac{1}{\exp\left(\frac{hc}{\lambda k T_{em}}\right)-1} \tag{50}$$

where $h = 6.626 \times 10^{-34}$(Js) is the Planck constant,T_{em} is the temperature of the emitter (K),λ is the wavelength (m), $c = 2.997 \times 10^8 (m/s)$ is the speed of light and $k = 1.381 \times 10^{-23}$(J/k) is the Boltzmann constant [44].

When the radiative energy reaches the filter, the wavelengths which have less energy than a certain amount reflected back to the emitter and others pass the filter. In the other word, just the radiations which their wavelength is less than a certain amount can reach the PV cells and the other ones returned back to emitter to keep its surface temperature at a high range. This certain wavelength is called the cut-off wavelength of filter, shown by λ_c (m) and it can be calculated using the following relation [45]:

$$\lambda_c = \frac{hc}{E_g} \tag{51}$$

E_g is the cell energy band gap and depends on the type of cell. The energy band gap and cut-off wavelength for silicon are 1.1 eV and 1.1 μm, respectively [45].

For the power that passes through the filter, the following relation can be expressed using the radiative spectrum for each cell is calculated by [45]:

$$P_{flt} = \varepsilon_{em} A \int_0^{\lambda_c} I_b(\lambda, T_{em}) d\lambda \tag{52}$$

where, A is the surface area of emitter (m^2) and ε_{em} is the radiative emissivity of the emitter, which depends on the material properties of the emitter. In this study, its value is taken as 0.9.

After all, the radiative energy reaches PV cells and electrical power generation occurs in this section [44]:

$$P_{el} = J_{sc} \times V_{oc} \times FF \times Num_{cell} \times A \tag{53}$$

Here Num_{cell} is the number of cells that used in TPV unit. J_{sc} is the short-circuit current $(\frac{A}{m^2})$ [45]:

$$J_{sc} = \int_{\lambda_{min}}^{\lambda_c} \frac{q_0 \lambda}{hc} EQE(\lambda) I_b(\lambda) d\lambda \tag{54}$$

where $q_0 = 1.602 \times 10^{-19} c$ is the elementary charge and EQE is the external quantum efficiency of PV cells which can be obtained by the Eq. (55) and the Table 7 [45].

$$EQE = A + B\lambda + C\lambda^2 + D\lambda^3 + E\lambda^4 + F\lambda^5 \tag{55}$$

λ_{min} is the minimum value of wavelength which PV cell gets and have the a relation with cut-off wavelength:

$$\lambda_{min} = \frac{\lambda_c}{2.5} \tag{56}$$

V_{oc} is the open circuit voltage (V) [45]:

$$V_{oc} = \frac{\Gamma k T_c}{q_0} \ln\left(\frac{J_{sc}}{J_0} + 1\right) \tag{57}$$

where, Γ is diode ideality factor and is assumed to be 1, T_c is the cell temperature and is considered 300 K in this study and J_0 is saturation current density and is obtained by the relation [45]:

$$J_0 = 1.5 \times 10^5 \exp\left(\frac{-E_g}{kT_c}\right) \tag{58}$$

Finally, FF is the dimensionless fill factor [45]:

$$FF = \beta \frac{\nu - \ln(\nu + 0.71)}{\nu + 1} \tag{59}$$

where β is the correction factor and is taken 0.96 here. ν is calculated by [45]:

$$\nu = \frac{q_0 V_{oc}}{kT_c} \tag{60}$$

Table 8 summarizes the assumptions applied in modeling the TPV subsystem.

3.6. Techno-economic analysis

Evaluating the feasibility, profitability, and cost-effectiveness of energy systems among similar technologies is of crucial significance in the field of techno-economic analysis.

$\dot{Z}$ represents the financial burden associated with capital investment, in addition to the operational and maintenance expenses related to each component of the system [27]:

$$\dot{Z}_k = Z_k^{CI} + Z_k^{OM} \tag{61}$$

In order to determine the value of $\dot{Z}_k$ using the available data on purchase equipment cost (PEC), one can employ the subsequent relationship [27]:

$$\dot{Z}_k = Z_k^{CI} + Z_k^{OM} = CRF \times TCI_k \times \left(\frac{24 \times 365}{N}\right) + \phi_r \times PEC_k \tag{62}$$

In the mentioned relationship, CRF represents the capital recovery factor, N denotes the number of annual operating hours of the system, bl indicates the useful life of the system, i signifies the interest rate, and the term ϕ_r also reflects the repair factor [27].

$$CRF = \frac{i(1+i)^n}{i(1+i)^n - 1} \tag{63}$$

While last, the costs associated with purchasing equipment have been revised to reflect the current year, utilizing the CEPCI [27]:

$$PEC_k = PEC \times \frac{CEPCI_{2022}}{CEPCI_{orginal}} \tag{64}$$

Table 9
Elements of the overall financial commitment [27].

Total Capital Investment (TCI)	Direct cost (DC	Onsite costs(ONSC)	Purchased −equipment cost(PEC)	1
			Purchased −equipmentinstallation (PEI) = 0.33 × PEC	2
			Piping = 0.35 × PEC	3
			Electrical equipmentand materials = 0.13 × PEC	4
		Offsite costs (OFSC)	Land = 0.05 × PEC	6
			Civil, structual, and architectural work = 0.21 × PEC	7
			Service facilities = 0.35 × PEC	8
		Indirect cost (IC)	Engineering and supervision = 0.08 × DC	9
			Construction costs including contracor's profit = 0.15 × DC	10
			Contingencies = 0.15 × (1.23 × DC)	11

Table 10
Assumptions for the economic analysis.

Parameter	Value	Unit	Reference
Plant expected life, bl	20	*year*	[24]
Annual number of hours, N	7000	*hour*	[24]
Maintenance factor, ϕ_r	1.06	–	[24]
Interest rate, i	15	%	[24]
LNG import price, c_{46}	6.982	$/GJ$	[49]
Digestion fuel price, c_1	11	$/GJ$	[50]
Hydrogen price, c_{37}	1.35	$/kg$	[51]
Carbon dioxside price, c_{53}	0.015	$/kg	[51]
LNG selling price, c_{48}	1.15	$/GJ$	[52]
Electricity price, c_{elec}	0.08	$/kWh$	[53]

the cost index for 2022 is 813 [46].

The overall expense rate of the multi-generation system stands at [47]:

$$\dot{Z}_{tot} = \sum \dot{Z}_k \tag{65}$$

The application of these economic analyses to the system components is detailed in Table S2 of the supplementary file [11,24,27,29,34,48].

Table 9 outlines the key components for calculating the total capital investment (TCI) of the proposed power generation system. The assessment of fixed investment expenses includes direct and indirect costs, with certain expenses omitted. The overall investment is determined by these costs [27]:

$$TCI = FCI + otheroutlays = DC + IC \tag{66}$$

Before investing in a project, it is essential to assess potential returns. The net present value (NPV) method is used to evaluate the economic feasibility of the proposed system by discounting the net cash flow at the end of each fiscal year to its present value using the current interest rate [27]:

$$NPV_{bl} = -TCI + \sum_{bl=0}^{bl} YIF_{bl} RDF_{bl} \tag{67}$$

In this context, i represents the interest rate, set at 15 %, while bl denotes the economic lifespan of the proposed facility, projected to be 20 years. Moreover, Y denotes the net cash flow at the conclusion of year bl, which is articulated as [24,27]:

$$Y = AI - (C^{O\&M} + C_f) \tag{68}$$

AI represents the annual income, while $C^{O\&M}$ denotes the costs associated with operating and maintenance, and C_f signifies the fuel cost. The definitions of these terms are as follows:

$$AI = c_{elec} \times N \times \dot{W}_{net} + c_{CO_2} \times N \times \dot{m}_{53} \times 3600 + c_{LNG} \times N \times \dot{E}_{48} \times 0,0036 + c_{H_2} \times N \times \dot{m}_{37} \times 3600 \tag{69}$$

$$C^{O\&M} = 0,06 \times PEC \tag{70}$$

$$C_f = \dot{C}_1 + \dot{C}_{46} \tag{71}$$

$$IF_{bl} = \left(1 + \left(\frac{i}{100}\right)\right)^{-bl} \tag{72}$$

$$RDF_{bl} = \left(1 + \left(\frac{Ri}{100}\right)\right)^{-bl} \tag{73}$$

The payback period (PBP) represents the essential duration required for the project's NPV to turn positive. The PBP of the reference system represents the duration needed for the NPV to surpass zero [27].

$$PBP = min\{bl : NPV(bl) > 0\} \tag{74}$$

Table 10 summarizes the assumptions applied in modeling the economic analysis.

3.7. Environmental analysis

In energy system evaluations, the ecological impacts of facilities are crucial. While transitioning from fossil fuels to renewable energy is common, it's important to recognize that renewable technologies can also have negative environmental effects. Exergo-environmental approaches, incorporating exergy-driven principles, help assess these impacts. One method to improve efficiency is by reducing exergy destruction, which lowers resource consumption while maintaining electricity production. Increased fuel consumption inevitably raises environmental consequences, as reflected by an indicator that highlights this relationship [54]:

$$\zeta = \frac{3600 \times \dot{m}_{53}}{\dot{m}_{H_2} \times LHV_{H_2} + \dot{W}_{net,Total}} \tag{75}$$

Eq. (75) defines the specific carbon emission index (ζ) of the system, expressed as the ratio between the CO_2 mass flow rate emitted to the environment and the total useful energy outputs of the system (i.e., hydrogen energy and net electricity). The numerator captures actual CO_2 emissions, while the denominator reflects the total energetic value of the outputs, providing a meaningful measure of carbon performance per unit of energy delivered.

3.8. Performace criteria

The calculation of system exergy efficiency is as follows:

$$(\eta_{II})_{total} = \frac{\dot{W}_{net,Total} + \dot{E}_{37} + \dot{E}_{53}}{\dot{E}_1 + \dot{E}_{46}} \tag{76}$$

The total unit cost associated with the product for the multi-generation system is equally articulated as:

$$C_{p,total} = \frac{\dot{C}_1 + \dot{C}_{46} + \dot{Z}_{tot}}{\dot{W}_{net,total} + \dot{E}_{37} + \dot{E}_{53}} \tag{77}$$

Table 11
The extensive array of decision variables inherent in the grey wolf algorithm methodology.

Decision variable	Unit	Lower bound	Upper bound
Output temperature of combustion chamber, T_{10}	K	1400	1600
Pressure ratio of compressors and turbines, Pr	–	9	25
Inlet turbine temperature, T_{38}	K	1000	1100
Current density of SOFC, j	A/m^2	6000	8000

3.9. Multi-objective optimization

The Grey Wolf Optimization (GWO) algorithm, introduced by Mir Jalali et al. [55] in 2014, draws inspiration from the social dynamics and collaborative strategies of grey wolves to tackle intricate optimization challenges. In the realm of multi-objective optimization, GWO is refined through the integration of Pareto front principles. Each solution, represented as a wolf, possesses an objective function vector to assess performance across various objectives. Solutions are systematically ranked, with non-dominated solutions occupying the forefront. The leading trio of wolves directs the remaining members, mirroring hunting behavior to uncover the optimal solution [55,56]:

$$\vec{D}_\alpha = \left| \vec{C}_1 \bullet \vec{X}_\alpha(t) - \vec{X} \right| \tag{78}$$

$$\vec{D}_\beta = \left| \vec{C}_2 \bullet \vec{X}_\beta(t) - \vec{X} \right| \tag{79}$$

$$\vec{D}_\delta = \left| \vec{C}_3 \bullet \vec{X}_\delta(t) - \vec{X} \right| \tag{80}$$

$$\vec{X}_1 = \vec{X}_\alpha - \vec{A}_1 \bullet \vec{D}_\alpha \tag{81}$$

$$\vec{X}_2 = \vec{X}_\beta - \vec{A}_2 \bullet \vec{D}_\beta \tag{82}$$

$$\vec{X}_3 = \vec{X}_\delta - \vec{A}_3 \bullet \vec{D}_\delta \tag{83}$$

$$\vec{X}(t+1) = \left(\vec{X}_1 + \vec{X}_2 + \vec{X}_3 \right)/3 \tag{84}$$

Here, t is the current iterations, $\vec{X}$ is the grey wolf's position vector and $\vec{A}$, $\vec{C}$ are coefficient vectors.

An external Pareto archive maintains the optimal non-dominated solutions, with the most favorable values of α, β, and δ chosen through a prominent strategy. To promote a balanced representation, the crowding distance concept is employed, facilitating an even distribution of solutions throughout the objective landscape. Two scenarios of multi-objective optimization are implemented:

1. The initial scenario enhances the emission index, maximizes net output power, and improves second law efficiency.
2. The second case enhances the emission index, maximizes net output power, and reduces the total unit cost of the product.

The initial scenario objectives focusing on sustainability, energy efficiency, and optimized thermodynamic performance. The second scenario emphasizing both environmental goals and economic feasibility for practical deployment.

The MOGWO method involves the establishment of decision-making parameters, with the relevant decision variables outlined in Table 11.

As indicated in Table 11, the output temperature of the combustion chamber (T_{10}) is set between 1400–1600 K to optimize combustion

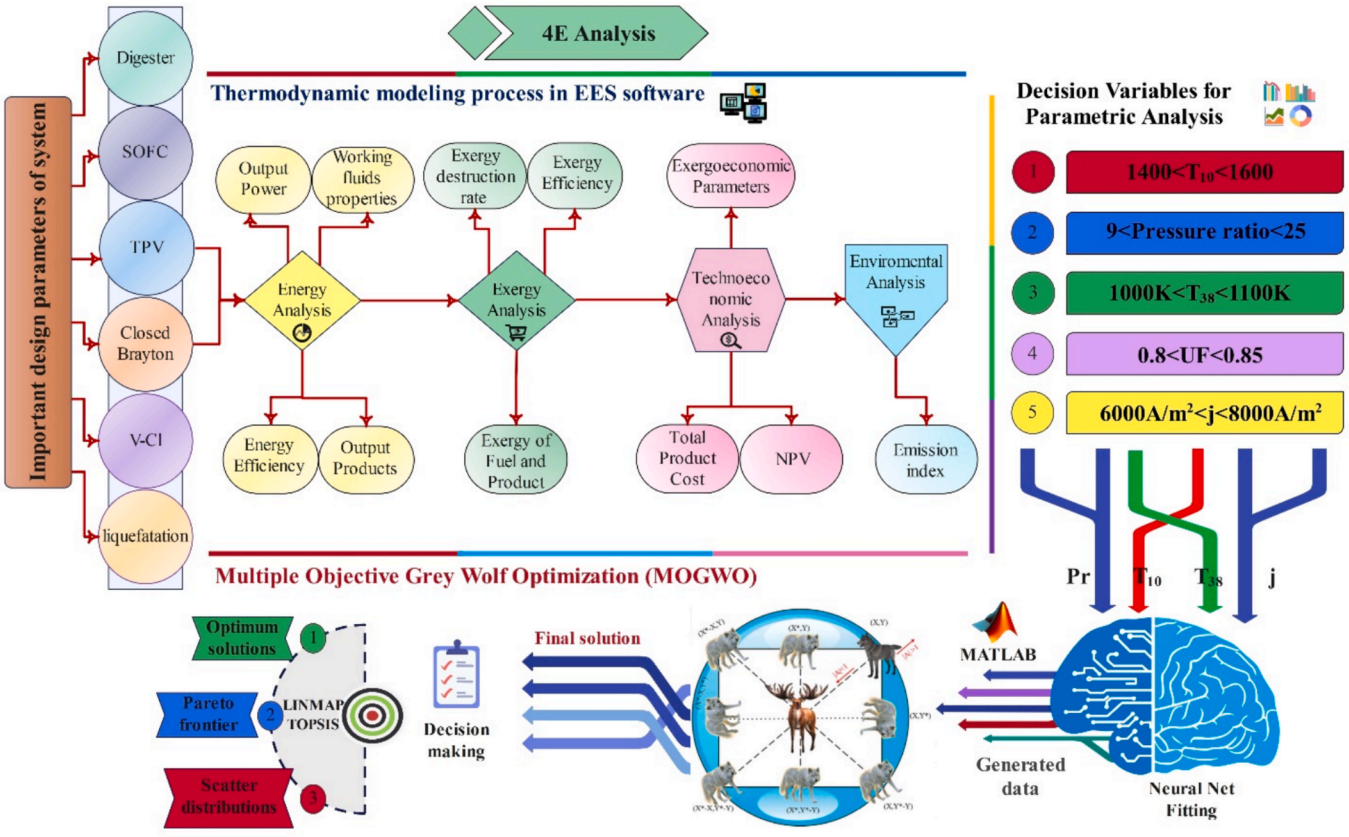

Fig. 3. Thorough strategies for modeling and optimization.

Table 12
Validation of solid oxide fuel cell unit.

$J(A/cm^2)$	$V_{cell}(V)$(Present study)	$V_{cell}(V)$(Tao et al. [57])	$V_{cell}(V)$(Yari et al. [22])	Densityofpower$\left(\frac{W}{m^2}\right)$(Present study)	Densityofpower(W/m^2)(Tao et al. [57])	Densityofpower(W/m^2)(Yari et al. [22])
0.2	0.787	0.76	0.742	0.154	0.15	0.148
0.3	0.702	0.68	0.684	0.215	0.21	0.205
0.4	0.64	0.62	0.634	0.251	0.26	0.253
0.5	0.551	0.57	0.582	0.283	0.295	0.294
0.6	0.513	0.52	0.547	0.304	0.315	0.328

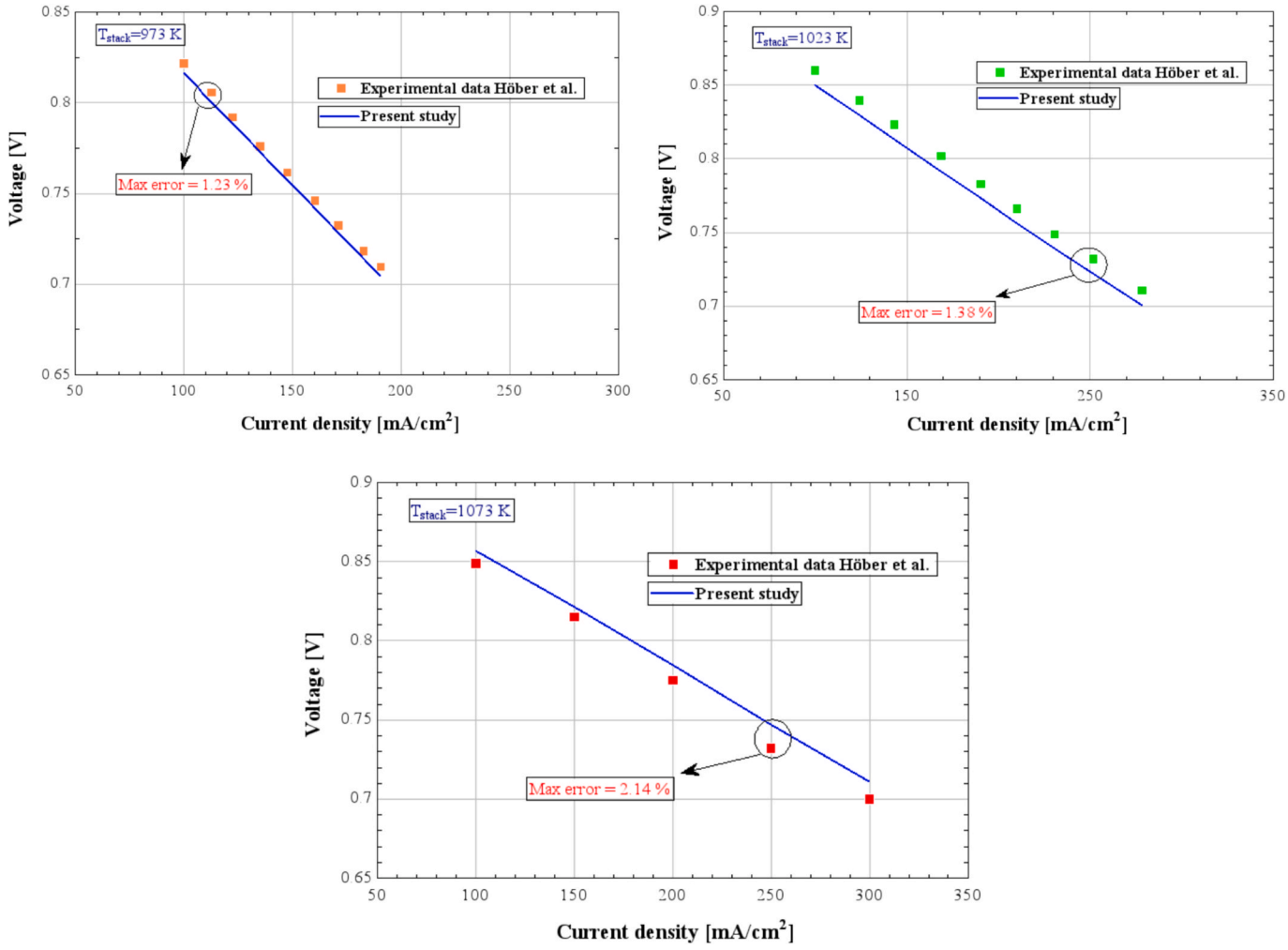

Fig. 4. The validation of SOFC unit with experimental data.

Table 13
. Validation of closed Brayton Cycle.

State	Pressure (kPa) (Present study)	Pressure (kPa) (ref [8])	Error (%)	Temperature (K) (Present study)	Temperature (K) (ref [8])	Error (%)	Enthalpy (kJ/kg) (Present study)	Enthalpy (kJ/kg) (ref [8])	Error (%)
1	7320	7320	0	1073	1073	0	4045	4045	0
2	2625	2630	0.19	735.7	736.2	0.1	2280	2283	0.13
3	2575	2580	0.19	424.1	424.1	0	662.9	662.9	0
4	2535	2540	0.19	350.71	350.73	0.02	281.8	282	0.07
5	2500	2500	0	303.27	303.27	0	35.44	35.46	0.05
6	4330	4330	0	385	386.5	1.33	465.4	473.3	1.69
7	4290	4290	0	344.09	345.63	2.16	253	261	3.16
8	4250	4250	0	302.61	302.76	0.5	37.65	38.45	2.12
9	7505	7500	0.06	387.3	389.1	1.57	487.7	496.7	1.84
10	7425	7420	0.06	700.8	701.4	0.14	2114	2117	0.14

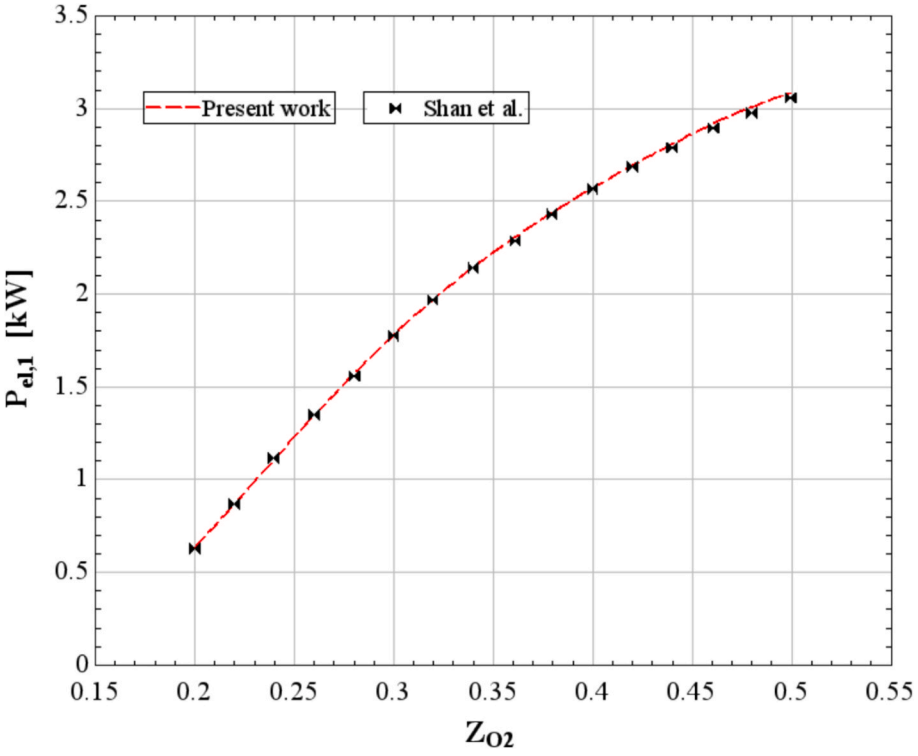

Fig. 5. Validation of thermophotovoltaic for the output power.

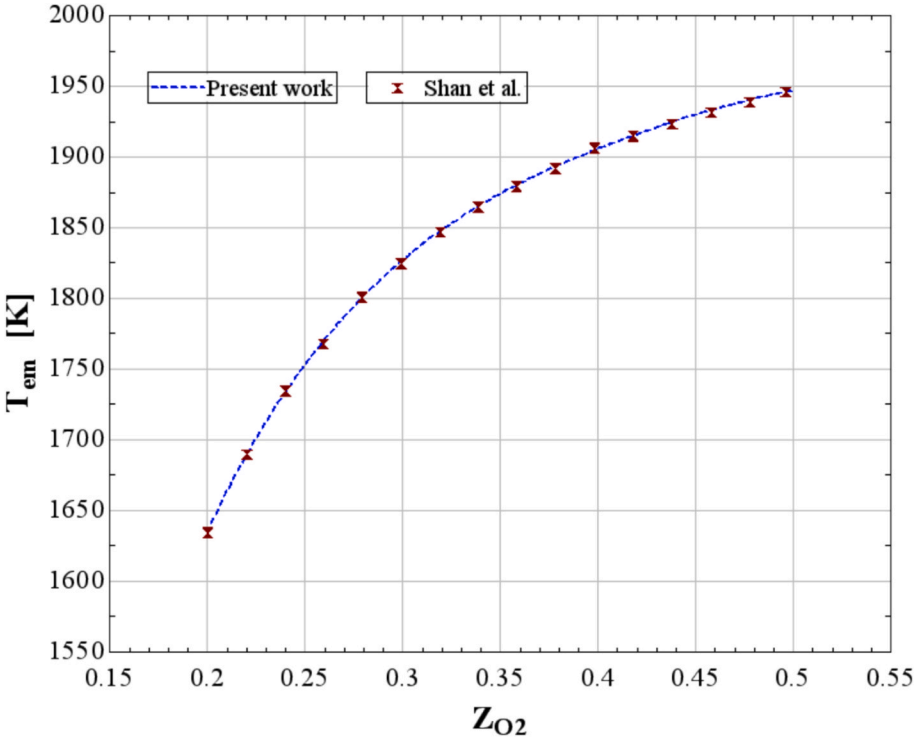

Fig. 6. Validation of thermophotovoltaic for the emitter temperature.

efficiency and power generation while maintaining thermal stability. The pressure ratio of compressors and turbines (PR) is chosen within 9–25 to ensure optimal thermodynamic efficiency in the SOFC and Brayton cycle, impacting both power generation and fuel efficiency. The inlet turbine temperature (T_{38}) is specified as 1000–1100 K to balance thermal efficiency with material integrity, ensuring safe and efficient turbine operation. Lastly, the current density of the SOFC (j) is set between 6000–8000 A/m^2 to achieve high energy density and performance, minimizing thermal degradation and efficiency losses.

Fig. 3 illustrates a comprehensive flowchart outlining the processes undertaken for the article. The process commences with a thorough examination of the multi-generation system, considering energy, exergy,

Table 14
Validation of vanadium chloride cycle.

Step number	Step temperature (K)	Reaction heat demand (kJ/mole H_2)		
		Balta et al. [11]	Present study	Error (%)
1	798	349.6	348.97	0.18
2	373	70.77	70.33	0.62
3	573	−88.72	−87.99	0.82

economic and environment factors. Subsequently, a comprehensive analysis is undertaken, leading to the refinement of the system through the utilization of MATLAB software.

4. Validation

The accuracy of the developed models has been verified by comparing their results with established experimental and numerical studies from the literature. The validation results for each subsystem are as follows:

4.1. Solid oxide fuel cell (SOFC) unit

To validate the SOFC sub-model, its predicted performance is compared with data from Tao et al. [57], which is based on experimental measurements, and Yari et al. [22], which provides results from a recent and well-validated simulation study. As shown in Table 12, the present model closely follows the cell voltage and power density trends reported in both sources across a range of current densities. The deviations are minimal, with voltage differences remaining within 5 %, supporting the model's consistency with both experimentally observed and independently simulated SOFC performance. Additionally, the exergy efficiency of the SOFC unit is calculated to be 48.9 %, which is in close agreement with the value reported by Sadeghi et al. [34] (47.9 %) in the optimization section of their study.

The developed SOFC model was validated using recent experimental polarization data reported by Höber et al. [58], which reflect state-of-the-art advancements in SOFC operating strategies. Validation was conducted for three stack operating temperatures of 973 K, 1023 K, and 1073 K, as illustrated in Fig. 4. In each case, the simulated voltage–current density relationship shows strong agreement with the experimental measurements, with maximum deviations of 1.23 %, 1.38 %, and 2.14 %, respectively. This close correlation across multiple operating temperatures confirms the model's capability to accurately reproduce the electrochemical behavior of modern SOFC systems, thereby ensuring that subsequent techno-economic and performance analyses are grounded in up-to-date technological data.

4.2. Closed Brayton Cycle

The validation of the Closed Brayton Cycle has been conducted using the study by Zare and Hasanzadeh [8]. Each state point in their article was simulated using Engineering Equation Solver (EES) software, and the results have been compared in Table 13. The table presents temperature, pressure, and enthalpy data for different states. The comparison indicates a minimal deviation between the present model and the results of Zare and Hasanzadeh [8], confirming the reliability of the model.

4.3. Thermophotovoltaic (TPV) unit

The Thermophotovoltaic (TPV) model has been validated using the study of Shan et al. [45]. The validation considers oxygen consumption (Z_{O_2}) for combustion and parametric analysis. The results focus on a single TPV unit used for combustion chamber waste heat utilization. The validation was performed by comparing the output power (P_{el}) and emitter temperature (T_{em}) with the findings of Shan et al. [45]. Figs. 5 and 6 illustrate the validation results for the output power and emitter temperature, showing that the plots closely align, confirming the model's accuracy with minimal error.

Table 15
The states supply details relevant to the current undertaking.

State	Workingfluid	T [K]	P [kPa]	$\dot{m}$[kg/s]	$\dot{Ex}$[kW]
1	Biomass	298.2	101.3	0.5	11,521
2	Biogass	328.2	101.3	0.5	10,438
3	Biogass	454.8	405.2	0.5	10,528
4	Biogass	454.8	405.2	0.315	6632
5	Biogass	454.8	393	0.185	3895
6	Air	298.2	101.3	5.957	0
7	Air	466.1	405.2	5.957	928.4
8	Air	466.1	405.2	4.687	730.4
9	Air	466.1	393	1.27	197.9
10	Combustion products	1500	393	5.003	5132
11	Combustion products	1229	393	5.003	3742
12	Combustion products	935.8	95.31	5.003	1790
13	Water	298.2	101.3	0.2097	0
14	Water	298.2	393	0.2097	0.06134
15	Water	1000	393	0.2097	289
16	Biogass	1000	393	0.185	4021
17	Air	1000	393	1.27	625.4
18	Water and Biogass	1000	393	0.3947	4310
19	Water and Biogass	1100	385.2	0.6227	1821
20	Air	1100	385.2	1.051	618.7
21	Exhaust gas	1561	381.3	1.674	2229
22	Exhaust gas	1230	95.31	1.674	1327
23	Exhaust gas	901.6	95.31	1.674	747.8
24	Combustion products and Exhaust gas	926.7	95.31	6.676	2509
25	Combustion products and Exhaust gas	673.2	95.31	6.676	1205
26	Combustion products and Exhaust gas except water	335.7	95.31	5.957	125.3
27	Vanadium chloride	798.2	101.3	2.88	893.8
28	Vanadium chloride	798.2	101.3	2.231	955.8
29	Chloride	798.2	101.3	0.649	131.5
30	Chloride	373.2	101.3	0.649	124.3
31	Water	373.2	101.3	0.1148	9775
32	Oxygen	373.2	101.3	0.102	1985
33	Hydrogen chloride	373.2	101.3	0.6618	169.9
34	Hydrogen chloride	573.2	101.3	0.6618	174.2
35	Vanadium chloride	573.2	101.3	2.231	920.1
36	Vanadium chloride	573.2	101.3	2.88	846.2
37	Hydrogen	573.2	101.3	0.01285	179.4
38	Helium	1073	7320	0.4184	1971
39	Helium	735.8	2625	0.4184	1212
40	Helium	424.3	2575	0.4184	886.8
41	Helium	310.8	2500	0.4184	834.2
42	Helium	394.4	4330	0.4184	1006
43	Helium	307.8	4250	0.4184	973.5
44	Helium	393.9	7505	0.4184	1152
45	Helium	701.6	7425	0.4184	1443
46	LNG	111.7	101.3	0.8225	888.4
47	LNG	112.8	3000	0.8225	892.3
48	LNG	290	3000	0.8225	424.5
49	Water	335.7	95.31	0.7194	4.732
50	Combustion products and Exhaust gas except water	567.5	524.2	5.957	1437
51	Combustion products and Exhaust gas except water	325.1	524.2	5.957	965.3
52	Nitrogen and Oxygen	206.9	524.2	5.213	886
53	Carbon dioxide	206.9	524.2	0.7444	414.4
54	Water	298.2	101.3	5.899	0
55	Water	308.2	101.3	5.899	4.045
56	Water	298.2	101.3	2.589	0
57	Water	308.2	101.3	2.589	1.775
58	Water	298.2	101.3	15.45	0
59	Water	338.2	101.3	15.45	159.3
60	Water	298.2	101.3	8.915	0
61	Water	338.2	101.3	8.915	91.92

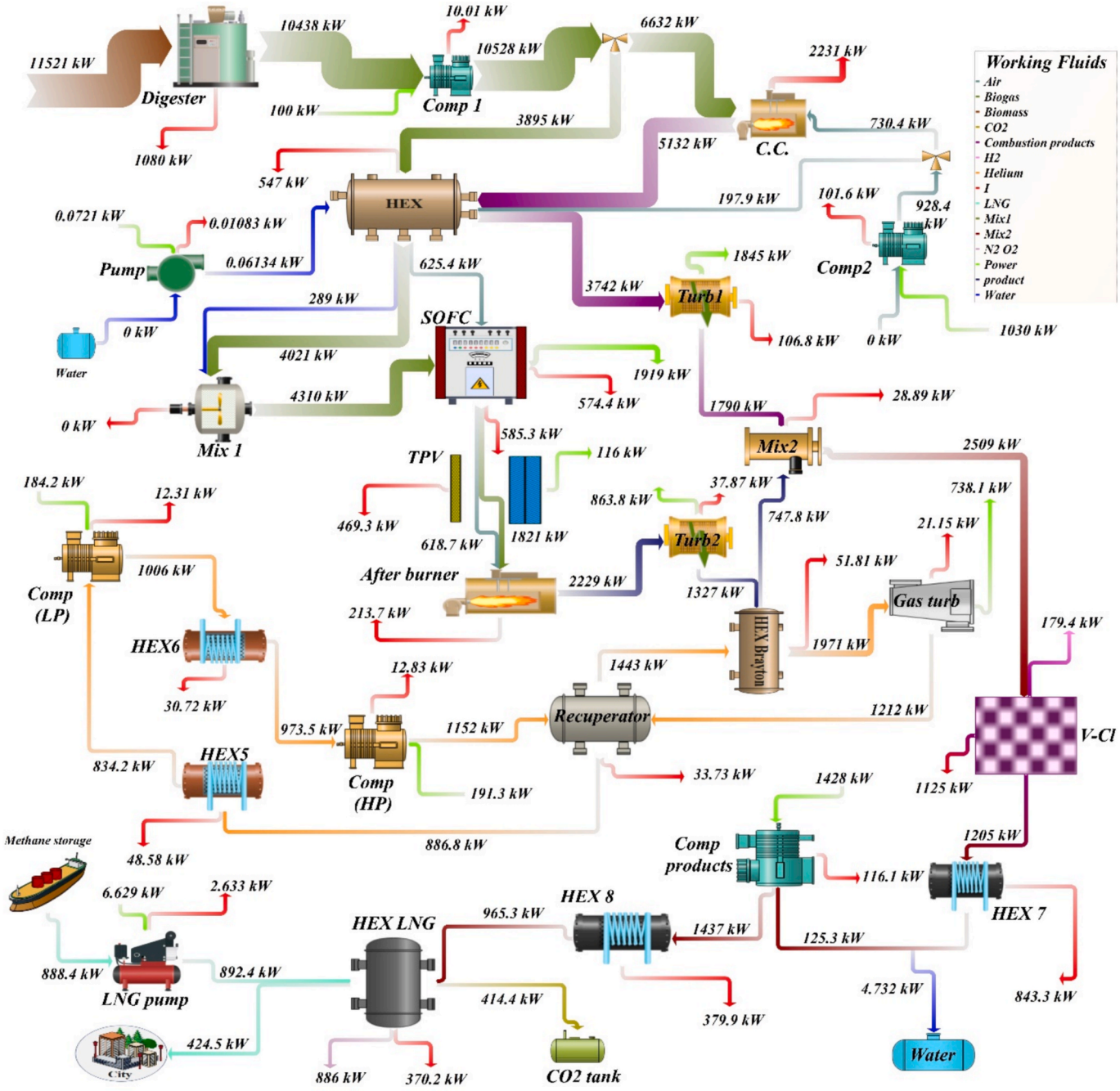

Fig. 7. The Sankey diagram of the system.

4.4. Vanadium chloride cycle

The Vanadium Chloride cycle model has been validated using the study conducted by Balta et al. [11]. The validation is based on three reaction steps, as detailed in Table 14. The key temperature values for each step are 798 K for the first step, 373 K for the second step, and 573 K for the third step. The reaction heat demand for each step was calculated and compared with the findings of Balta et al. [11]. The maximum observed error in the comparison was 0.82 %, indicating a high level of accuracy.

5. Results

The findings derived from the utilized methodologies, encompassing comparative assessments, parametric investigations, optimization results, and evaluations in base-mode operation, are outlined in this section. The findings are meticulously categorized into separate sections for comprehensive analysis.

5.1. Base-mode results

The base-mode conditions were chosen based on the assumptions specified for each subsystem. These assumptions reflect typical operating conditions for the target applications, ensuring the system's performance aligns with practical and feasible energy generation standards. The chosen conditions are designed to represent realistic scenarios, based on literature and industry practices, and provide a balanced approach to optimizing both efficiency and sustainability.

Table 16
Outcomes of the exergy assessment concerning the components of a multi-generation system.

Component	$\dot{E}x_F$ [kW]	$\dot{E}x_P$ [kW]	$\dot{E}x_D$ [kW]	ε [%]
Digestion				
Comp1	100	90.01	10.04	89.97
Comp2	1030	928.4	101.6	90.14
Digester	11,521	10,438	1084	90.6
CC	7363	5132	2231	69.71
Turb1	1952	1845	106.8	94.53
Solid oxide fuel cell (SOFC)				
Pump	0.07217	0.06134	0.01083	85
HEX	9225	8678	547	94.07
SOFC	4936	4361	574.4	88.36
After burner	2443	2229	213.7	91.25
Turb2	901.6	863.8	37.87	95.8
Mixer1	4310	4310	0	100
Mixer2	2538	2509	28.89	98.86
Closed Brayton cycle				
HEX Brayton	579.6	527.7	51.81	91.06
Gas turb	759.2	738.1	21.15	97.21
Comp HP	191.3	178.5	12.83	93.29
Comp LP	184.2	171.9	12.31	93.32
HEX5	886.8	838.2	48.58	94.52
HEX6	1006	975.3	30.72	96.95
Recuperator	2364	2330	33.73	98.57
Vanadium chloride cycle				
VCl	2509	1384	1125	55.16
Thermophotovoltaic (TPV)				
TPV	585.3	116	469.3	19.82
Liquefaction				
HEX7	1205	361.2	843.3	29.98
HEX8	1437	1057	379.9	73.57
HEX LNG	1858	1487	370.2	80.07
Comp products	1428	1312	116.1	91.87
LNG pump	6.629	3.996	2.633	60.28

5.1.1. Thermodynamic analysis

Table 15 presents comprehensive insights into the streams within the proposed framework. It encompasses fundamental components including working fluid, temperature, pressure, concentration, mass flow rate, and exergy rate. The information presented here forms a crucial foundation for the analyses undertaken, providing an in-depth examination of the operational characteristics of each stream. The Table 15 content significantly contributes to a comprehensive understanding of the system's overall dynamics and efficiency, providing it essential for a meticulous assessment from both thermodynamic and economic viewpoints.

5.1.2. Sankey diagram

Fig. 7 presents the Sankey diagram of the system, illustrating the distribution of energy and mass flows across its components. The diagram highlights the flow of biogas and air through compression, combustion, and the SOFC unit, with energy recovery stages including gas turbines, a closed Brayton cycle, and a TPV unit. Additionally, it depicts the integration of hydrogen production via the vanadium chloride cycle and CO_2 capture from the exhaust gases. The width of each stream represents the magnitude of energy or mass flow, providing a clear visualization of the system's energy utilization, conversion efficiencies, and losses. The CC contributes the most to exergy destruction at 2231 kW, followed by the VCl cycle at 1125 kW, and the digester at 1084 kW. These components experience high exergy losses due to irreversibilities in the combustion process, inefficient heat recovery, and energy conversion losses. These components are highly irreversible in terms of thermodynamic performance, leading to significant exergy losses, similar to what is observed in other literature on conventional systems. By integrating advanced heat recovery and multi-generation strategies, our system addresses these inefficiencies better than traditional setups.

The results derived from the examination of the multi-generation system components, encompassing fuel exergy, product exergy, exergy destruction, and exergy efficiency, are presented in Table 16.

5.1.3. Economic analysis

Economic analysis is crucial for evaluating the feasibility and profitability of the proposed system, ensuring that the investment is financially viable. By assessing key metrics such as Net Present Value (NPV), payback period, and cost distribution, stakeholders can determine the system's economic sustainability and return on investment. The analysis also helps identify the impact of electricity prices, hydrogen production, and CO_2 capture incentives on overall profitability. Additionally, it guides optimization efforts to minimize costs while maximizing revenue streams, making the system more competitive in the energy market.

Fig. 8 presents the pie chart of the system's capital cost distribution for 20-year, illustrating the contribution of each major component to the total investment. The chart highlights the SOFC unit as the most significant cost contributor, reflecting its advanced materials and high operating temperature requirements. The gas turbines and compressors also account for a substantial portion, given their role in energy conversion and system pressurization. The TPV unit, Brayton cycle, and CO_2 capture system contribute smaller but notable shares, emphasizing the additional investment needed for enhanced efficiency and emissions control. Meanwhile, the hydrogen production unit (vanadium chloride cycle) represents another key cost factor due to its specialized equipment and thermal energy demands. The chart provides insight into the financial feasibility of the system, emphasizing the cost distribution among power generation, waste heat recovery, and sustainability-enhancing components.

Fig. 9(a) illustrates the Net Present Value (NPV) trends of the proposed system over a 20-year operational period for electricity selling prices of 0.06 $/kWh, 0.08 $/kWh, and 0.12 $/kWh. In line with the practical lifespan limitations of solid oxide fuel cell stacks, the analysis includes replacement costs for an additional SOFC unit after the first 10 years of operation, resulting in a doubling of the SOFC capital cost in the long-term scenario. The initial negative NPV is attributed to the fixed capital investment, followed by an upward trend as revenues accumulate. Payback periods are 6.86 years for 0.12 $/kWh, 13.76 years for 0.08 $/kWh, and non-achievable within 20 years for 0.06 $/kWh.

Fig. 9(b) presents the corresponding NPV analysis for a 10-year operational period, in which the system cost includes only a single SOFC unit. The payback times are 3.54 years for 0.12 $/kWh, 5.4 years for 0.08 $/kWh, and 7.43 years for 0.06 $/kWh. The fixed capital investment for the 20-year scenario is approximately 11 M$, compared to 7 M$ for the 10-year case. Incorporating the replacement costs in the 20-year scenario increases the levelized product cost by approximately 4 %, from 48.23 $/GJ to 50.15 $/GJ. However, given the relatively small impact of this increase, the parametric analysis focuses on the one-unit case to illustrate the general techno-economic trends. The results highlight the economic viability of the system, emphasizing that profitability is highly dependent on electricity pricing, with higher prices significantly reducing the payback period and improving long-term financial performance.

5.1.4. The overall results

A comprehensive thermodynamic, economic, and environmental analysis has been conducted to evaluate the proposed system's performance. The system achieves a net power output of 2,542 kW, with a second law efficiency of 25.27 %. Additionally, hydrogen production reaches 0.01285 kg/s, contributing to the system's multi-generation capability. The hydrogen production rate for the specific heat input of 2,088 kW is 0.01285 kg/s which is in line with the production rate of the similar VCl cycle thatis studied by Javaherian et al. [59] (0.018 kg/s for approximitly 3 MW).

From an exergo-economic perspective, the unit exergy cost of total products is 48.23 $/GJ, demonstrating the system's cost-effectiveness. The environmental impact is significantly reduced, as the CO_2 emission index is 0.6562 kg/kWh when liquefaction is not applied. However,

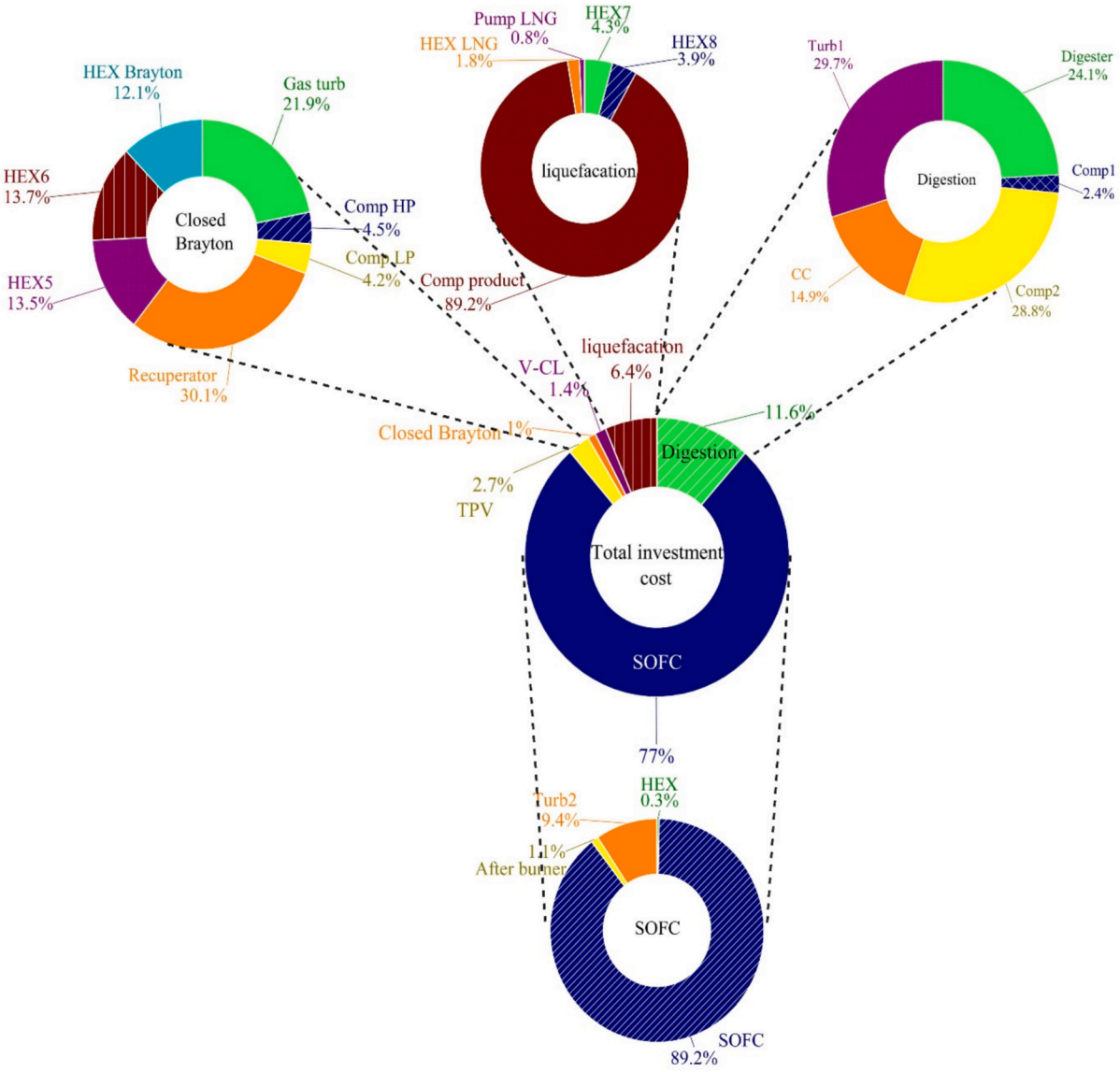

Fig. 8. The pie chart of the system's capital cost distribution for 20-year (includes SOFC replacement cost).

through CO_2 liquefaction at a rate of 0.7444 kg/s, the system minimizes emissions, making it an environmentally friendly solution.

the exergoeconomic performance of the proposed system is compared with a recent theoretical study by Laleh et al. [60], which integrates photovoltaic thermal panels, a proton exchange membrane electrolyzer, a solid oxide fuel cell, a biomass gasifier, and a Rankine cycle. Their system reports a total product cost of 34.7 $/GJ, whereas the proposed system reaches 48.23 $/GJ, primarily due to the inclusion of a CO_2 liquefaction unit that enhances environmental performance. Despite the higher cost, the present system demonstrates superior productivity, achieving a net output power of 2,542 kW (compared to 1,395 kW), a hydrogen production rate of 0.01285 kg/s (vs. 0.004 kg/s), and a higher SOFC exergy efficiency of 40.08 % (vs. 24.88 %). These results highlight the thermodynamic and environmental advantages of the proposed configuration.

To further enhance efficiency, a thermophotovoltaic (TPV) unit is integrated to utilize the high waste heat from the SOFC, generating additional power and improving overall performance. Given these advantages, the proposed system proves to be an efficient, sustainable, and eco-friendly solution for energy production.

5.2. Parametric study

A parametric study is essential for understanding the impact of key design and operating parameters on the performance, efficiency, and sustainability of the proposed system. By analyzing variables such as compressor pressure ratio, combustion chamber temperature, SOFC current density, and fuel utilization factor, the study helps identify optimal conditions that maximize power generation, hydrogen production, and CO_2 capture while minimizing costs and environmental impact. It also provides insights into system behavior under different scenarios, enhancing flexibility and adaptability for real-world applications. Ultimately, parametric analysis guides multi-objective optimization, ensuring a well-balanced trade-off between economic, environmental, and operational factors.

Fig. 10 (a with TPV and b without TPV unit) shows the variation of net generated power ($\dot{W}_{net}$), exergy efficiency, captured CO_2 mass flow rate ($\dot{m}_{53}$), environmental index, hydrogen production ($\dot{m}_{37}$), and total cost of products (Cp) with respect to the pressure ratio of air and biogas compressors.

As the pressure ratio increases, both $\dot{W}_{net}$ and exergy efficiency exhibit an upward trend, indicating improved energy conversion and

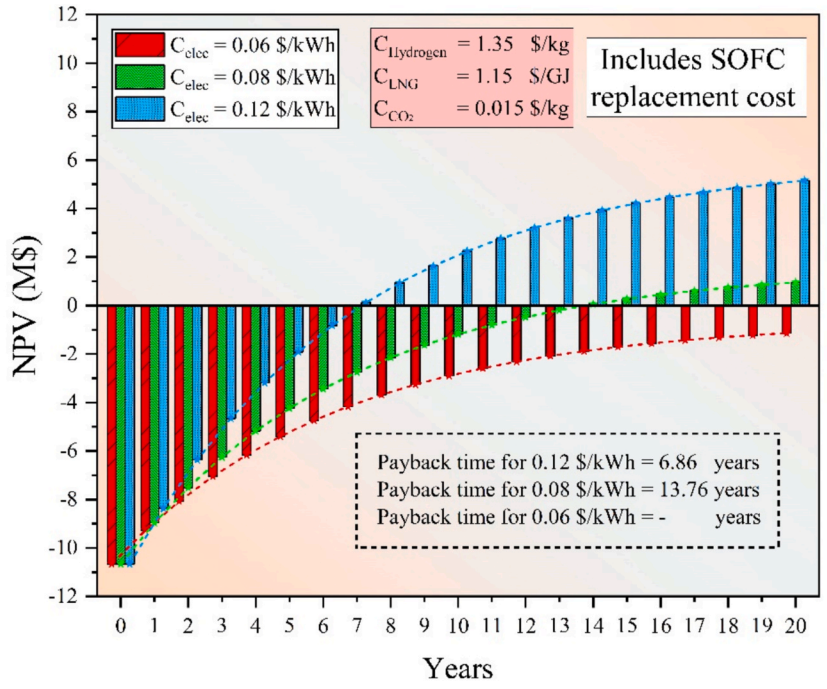

(a)

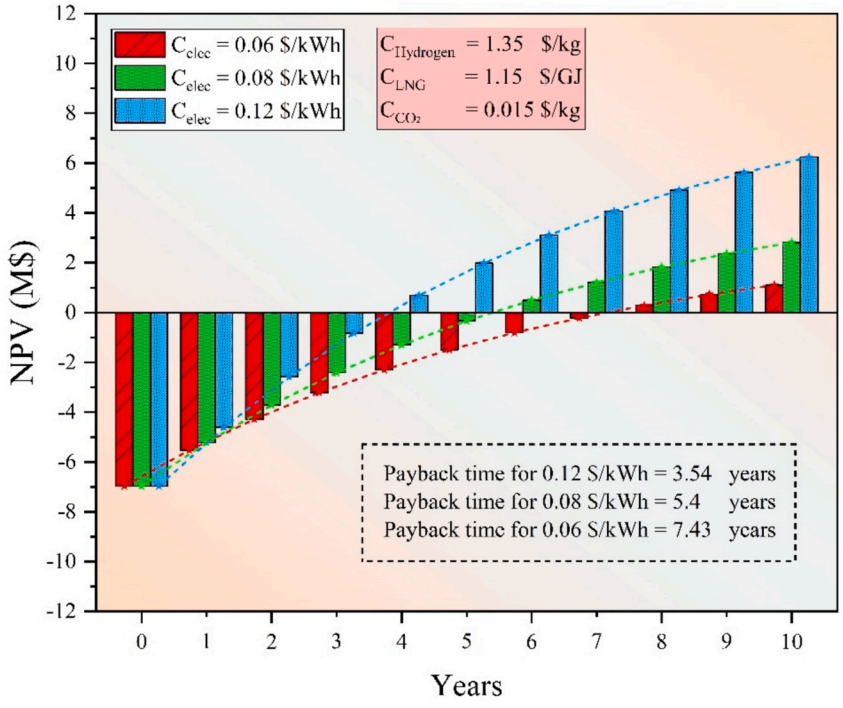

(b)

Fig. 9. The net present value analysis of the system over 20 (includes SOFC replacement cost) and 10 years for different electricity selling prices.

system performance. Similarly, the amount of captured CO_2 ($\dot{m}_{53}$) rises, the air–fuel ratio increases. The reason for this behavior is that with elevated compression rates, expansion in the gas turbines alongside higher mass flow rate due to elevation in air–fuel ratio leads to higher power generation that covers the extra power consumption in the compressors. On the other hand, the environmental index, hydrogen production ($\dot{m}_{37}$), and total cost of products (Cp) decrease, suggesting that higher pressure ratios make the system more environmentally friendly and cost-effective, but slightly reduce hydrogen generation due to shifting energy utilization toward power production. Notice that the environmental index drop is affected by the increase in power generation, albeit the CO_2 rate increase, which shows that the increased output

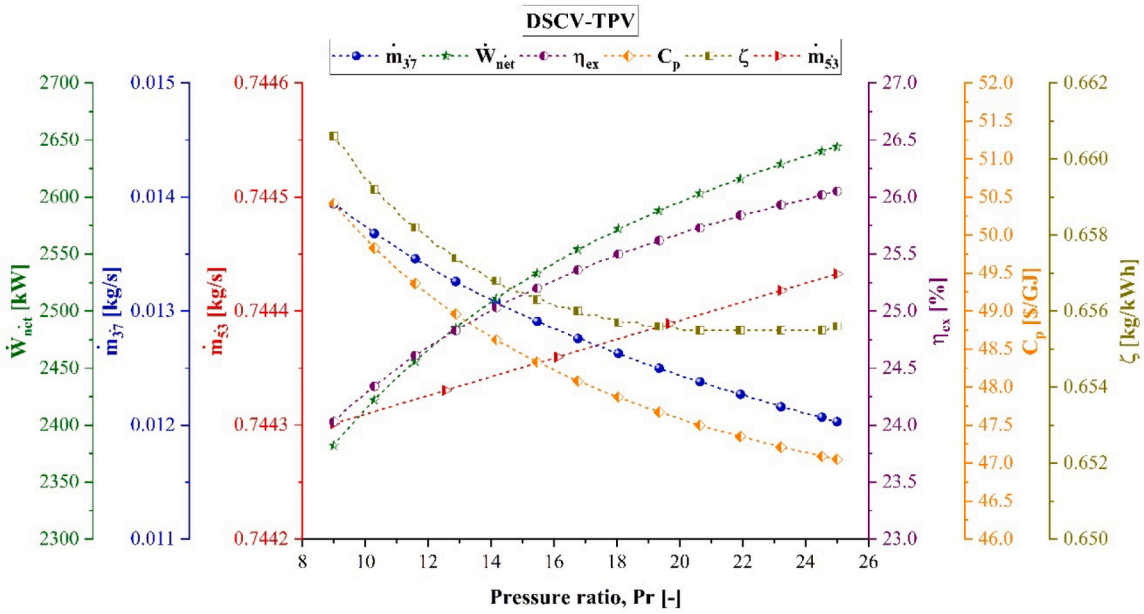

(a)

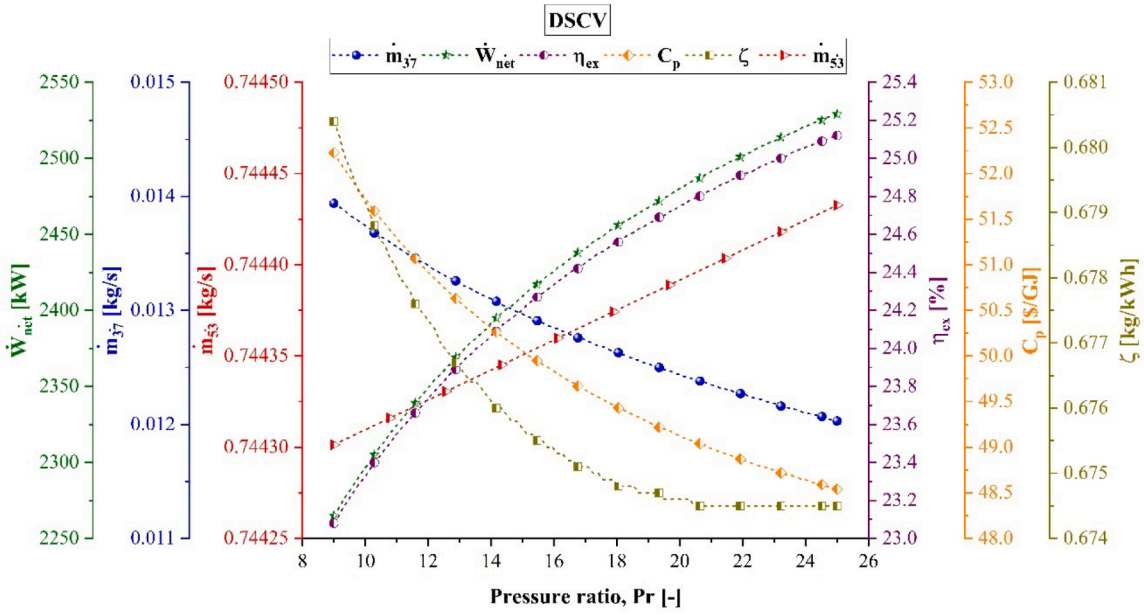

(b)

Fig. 10. The variation of the key indicators of the system versus the compressor's pressure ratio.

of the system is overall beneficial.

The difference between layouts (a) and (b) in this figure is noticeable across all parameters. With the TPV unit (Figure a), the system consistently outperforms the one without TPV (Figure b) in terms of power generation, efficiency, and cost reduction. The TPV unit enhances overall performance by recovering radiation losses from the SOFC, leading to greater energy utilization and sustainability.

Fig. 11 (a with TPV and b without TPV) illustrates the effect of combustion chamber temperature on key system parameters, including $\dot{W}_{net}$, exergy efficiency, hydrogen production, environmental index, captured CO_2, and Cp.

As the combustion chamber temperature increases, $\dot{W}_{net}$, exergy efficiency, and hydrogen production rise in both layouts. The increase in $\dot{W}_{net}$ is due to improved thermal energy availability, which enhances the performance of downstream components such as the gas turbines and SOFC. Higher combustion temperatures also improve exergy efficiency

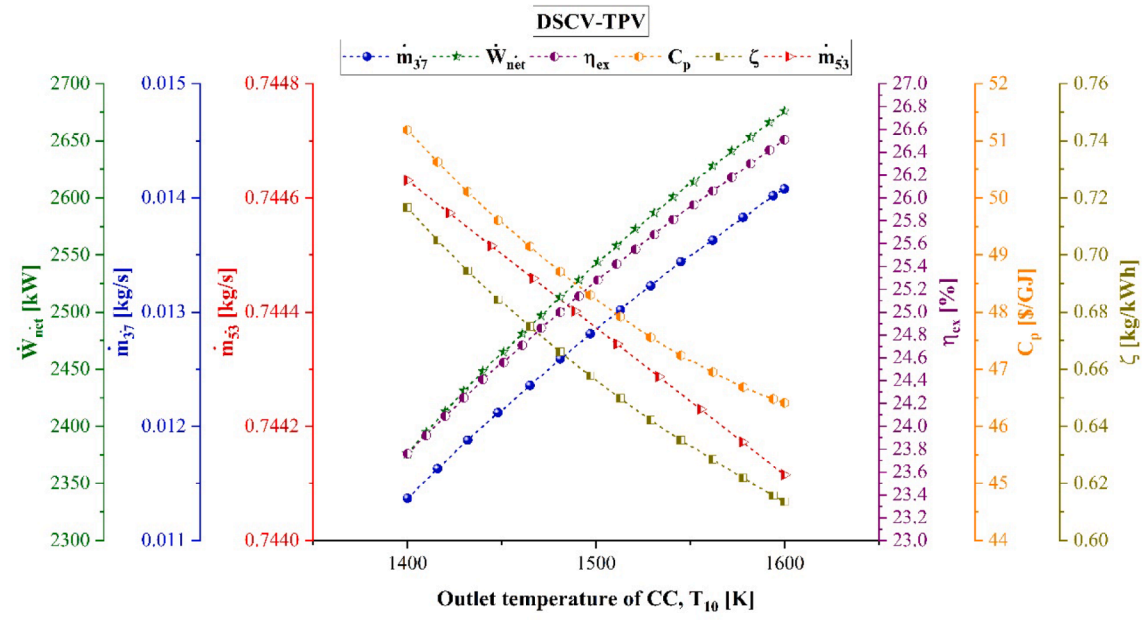

(a)

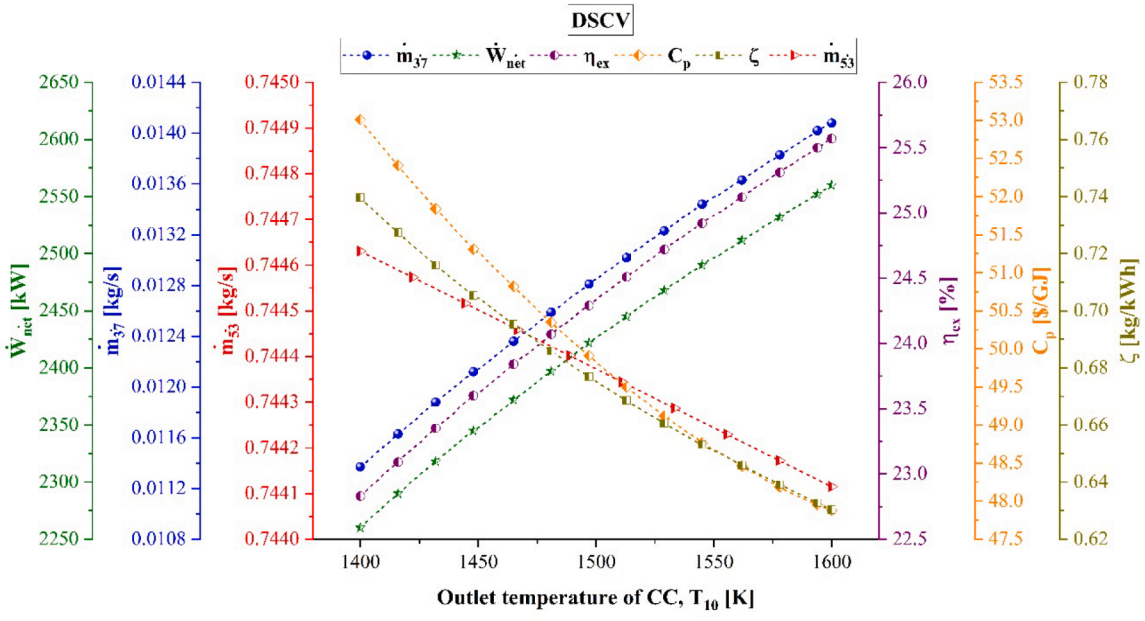

(b)

Fig. 11. The variation of the key indicators of the system versus the combustion chamber temperature.

by reducing entropy generation and increasing useful work output. The rise in hydrogen production is attributed to the higher thermal energy available for the vanadium chloride cycle, which relies on high temperatures to drive endothermic reactions for hydrogen production, as the pressure ratio is considered to be constant in this figure. Also, the downstream closed Brayton cycle benefits from the higher energy rate available as the VCl cycle works in strict temperature values.

Conversely, the environmental index, the amount of captured CO_2, and Cp decrease with temperature. The environmental index declines because the system generates more power relative to emissions, improving sustainability. The slight reduction in CO_2 capture occurs because higher combustion temperatures shift the reaction equilibrium, which leads to lower air injection into the combustion chamber. The decrease in Cp suggests that at higher temperatures, the system operates more efficiently, reducing the cost per unit of useful output. With the lower air flow rate, the expenses considered for compressors, heat exchangers, and turbines are lowered, while having an elevation in power production leads to more beneficial commodity production.

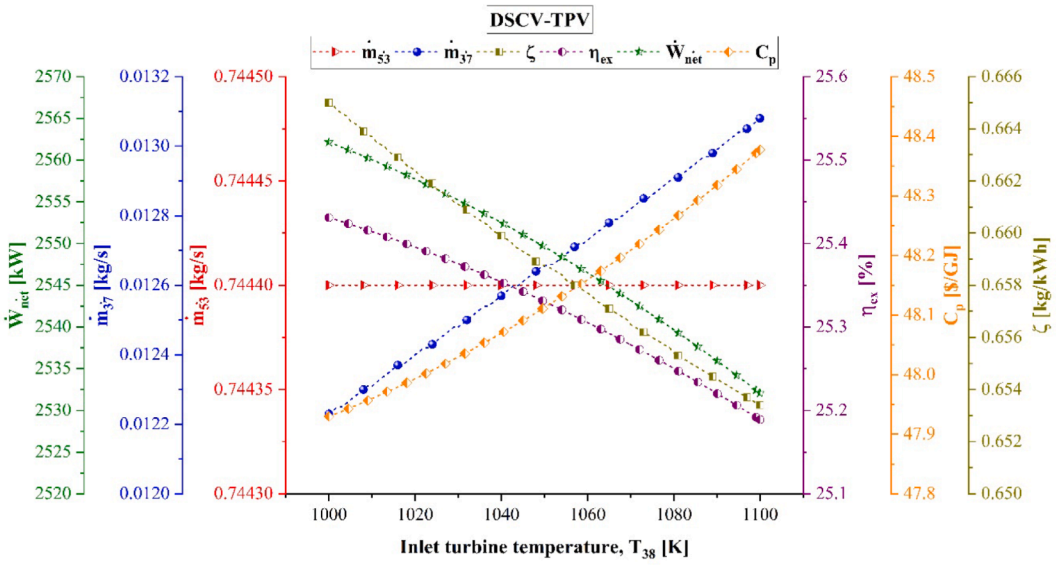

(a)

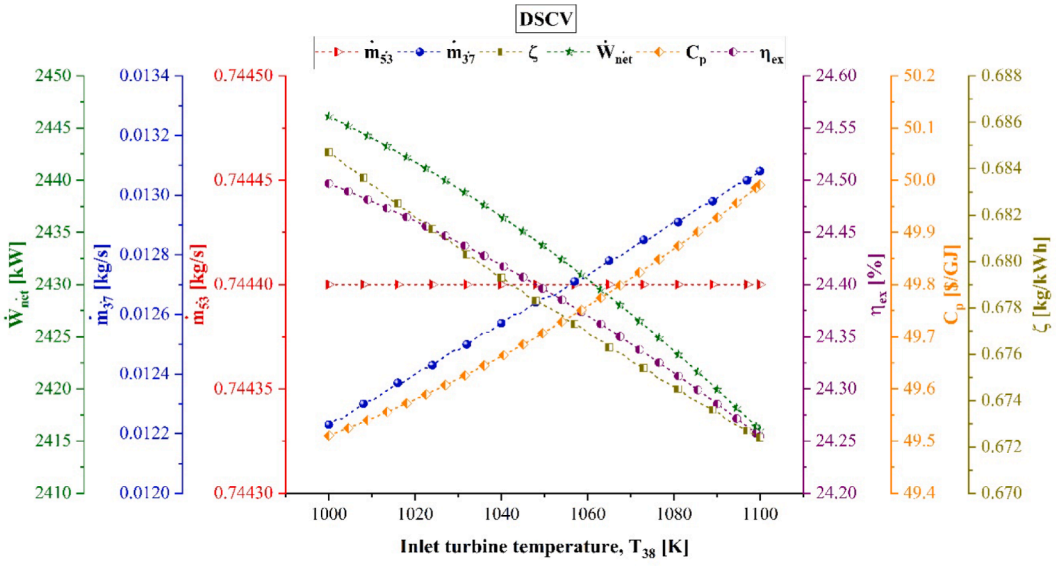

(b)

Fig. 12. The variation of the key indicators of the system versus the effect of Brayton cycle turbine inlet temperature.

The trends in layouts (a) and (b) in this figure follow a similar pattern, but Figure (a) (with TPV) consistently shows superior performance across all metrics. The TPV unit enhances power generation by capturing radiation heat loss from the SOFC and converting it into additional electricity. This extra power increases overall system efficiency, allowing for better fuel utilization and cost reduction as the rate of biogas fed to the SOFC unit is deemed to be fixed.

Overall, the system with TPV outperforms the system without TPV in every aspect, demonstrating that incorporating thermophotovoltaic technology improves energy recovery, economic feasibility, and environmental performance.

Fig. 12 (a with TPV and b without TPV) illustrates the effect of Brayton cycle turbine inlet temperature on key system parameters, including $\dot{W}_{net}$, exergy efficiency, environmental index, hydrogen production, captured CO_2, and Cp.

As the Brayton cycle turbine inlet temperature increases, $\dot{W}_{net}$ and exergy efficiency decrease in both Figures. This decline occurs because higher turbine inlet temperatures reduce the closed Brayton cycle flowrate and provides,ore heat and energy for VCl cycle. The environmental index also decreases, indicating a relative decrease in emissions, which remains constant per unit of power output.

On the other hand, hydrogen production and Cp increase. The rise in hydrogen production is due to the additional thermal energy available for the vanadium chloride cycle, which relies on high temperatures for efficient hydrogen generation. However, this increased hydrogen production comes at the expense of overall system efficiency, leading to

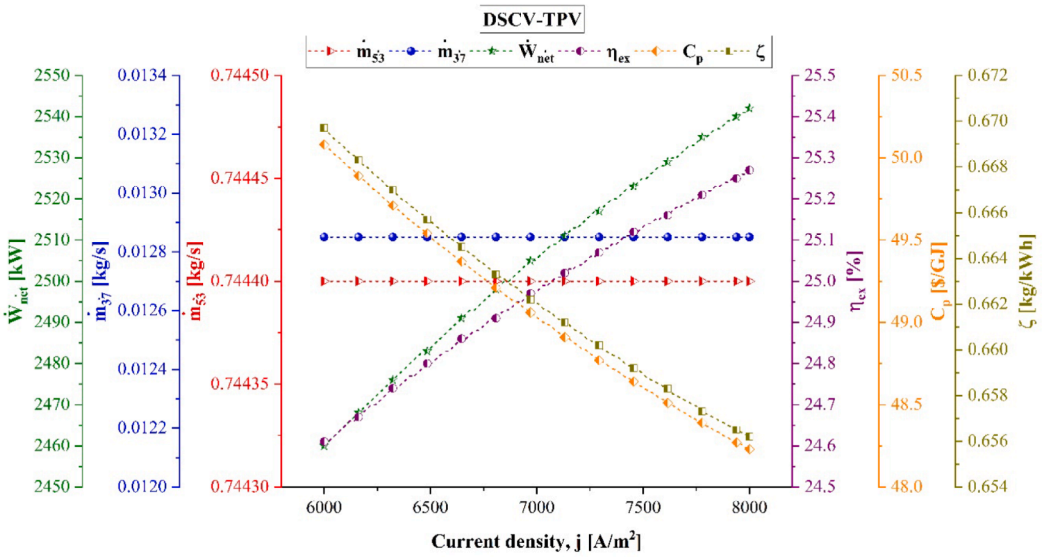

(a)

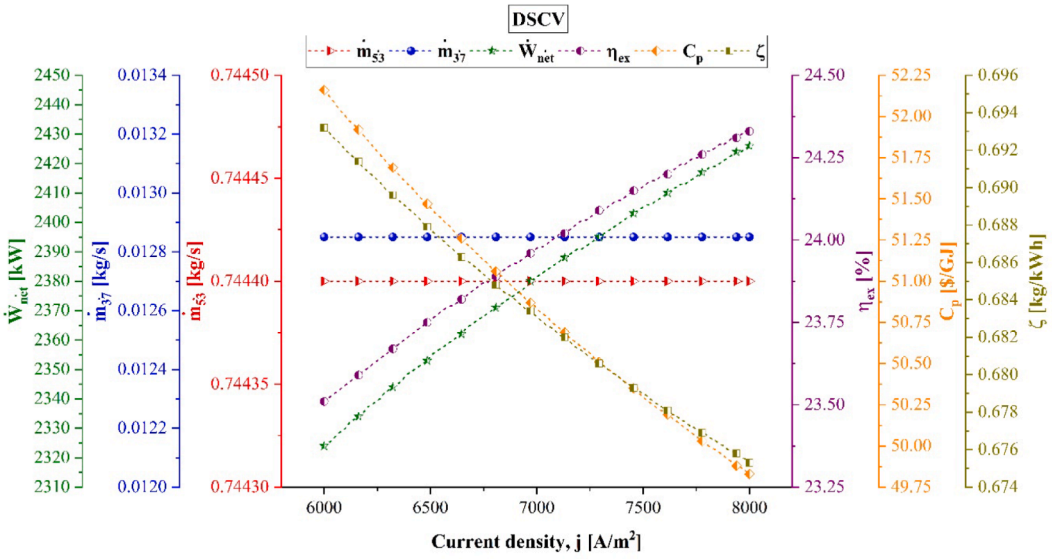

(b)

Fig. 13. The variation of the key indicators of the system versus the SOFC current density.

higher costs. Cp increases because the reduced efficiency leads to lower power generation, spreading fixed costs over a smaller energy output.

Interestingly, the amount of captured CO_2 remains constant across all temperature values. This suggests that CO_2 separation processes are independent of the Brayton cycle turbine inlet temperature, as the conditions affecting CO_2 capture remain unchanged.

Both layouts (a) and (b) in this figure exhibit similar trends, but Figure (a) consistently outperforms Figure (b) in all aspects as described above.

Fig. 13 (a with TPV and b without TPV) illustrates the effect of SOFC current density (j) on key system parameters, including $\dot{W}_{net}$, exergy efficiency, environmental index, Cp, captured CO_2, and hydrogen production rate.

As the j increases, $\dot{W}_{net}$ and exergy efficiency exhibit an upward trend in both Figures. Increasing the current density in a solid oxide fuel cell enhances power production because it raises the rate of electrochemical reactions, allowing more electrons to flow through the external circuit per unit area. Since power density is the product of cell voltage and current density, a higher current density generally leads to greater power output. However, this comes with increased polarization losses (activation, ohmic, and concentration losses), which slightly reduce the cell voltage. Despite this, up to a certain limit, the net effect is a rise in power output, making higher current densities desirable in SOFC operation.

Conversely, the environmental index and total cost of products (Cp) decrease as current density rises. The decline in the environmental index

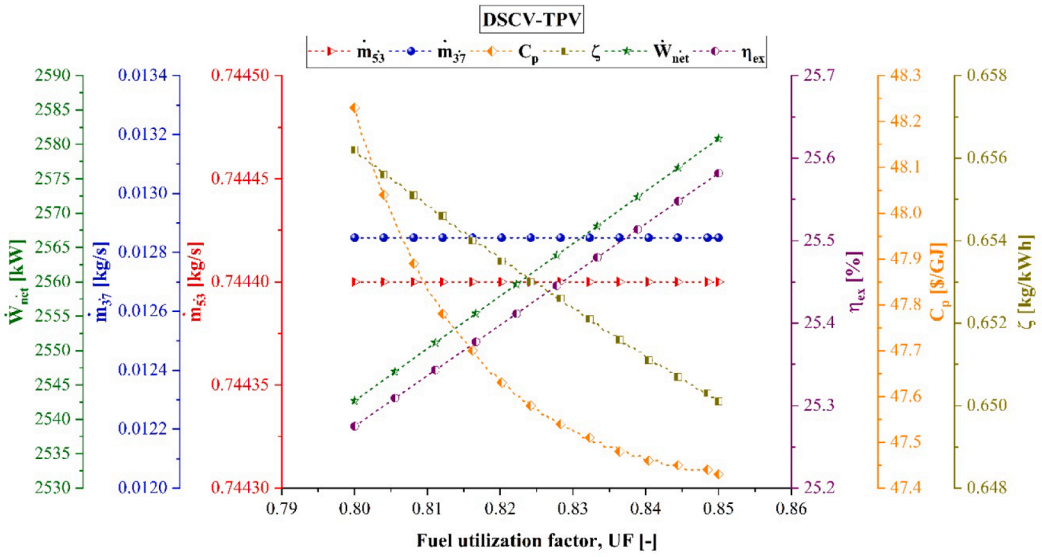

(a)

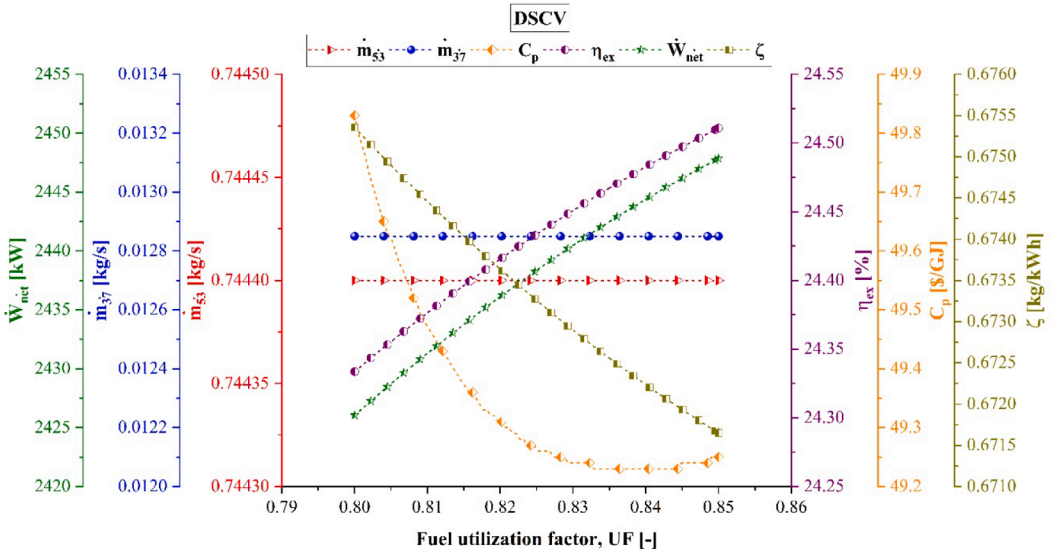

(b)

Fig. 14. The variation of the key indicators of the system versus the SOFC fuel utilization factor.

indicates a more sustainable operation, as the system generates more power with the same fuel input, reducing emissions per unit of energy produced. Meanwhile, the drop in Cp suggests that the system becomes more cost-effective as increased power generation leads to better utilization of resources, lowering the cost per unit of output.

Interestingly, the amounts of captured CO_2 and hydrogen production remain constant, meaning that changes in SOFC current density do not significantly affect the CO_2 capture process or hydrogen generation. This suggests that these parameters are more dependent on other system conditions, such as fuel composition and reaction temperatures, rather than electrochemical operating conditions.

Both layouts (a) and (b) in this figure display similar trends, but Figure (a) consistently shows better performance in all aspects as these studies are monitored based on the performance of the system as a unit.

Overall, increasing the SOFC current density improves power generation, efficiency, and sustainability while reducing costs, with the TPV-integrated system consistently outperforming the non-TPV system.

Fig. 14 (a with TPV and b without TPV) illustrates the effect of SOFC fuel utilization factor (UF) on key system parameters, including $\dot{W}_{net}$, exergy efficiency, environmental index, Cp, captured CO_2, and hydrogen production.

As the fuel utilization factor increases, $\dot{W}_{net}$ and exergy efficiency follow an upward trend in both Figures. Increasing the fuel utilization factor in an SOFC improves power output because it means a greater fraction of the supplied fuel is being electrochemically converted into electricity rather than exiting unreacted. As more fuel participates in the electrochemical reactions, more electrons are released, increasing the

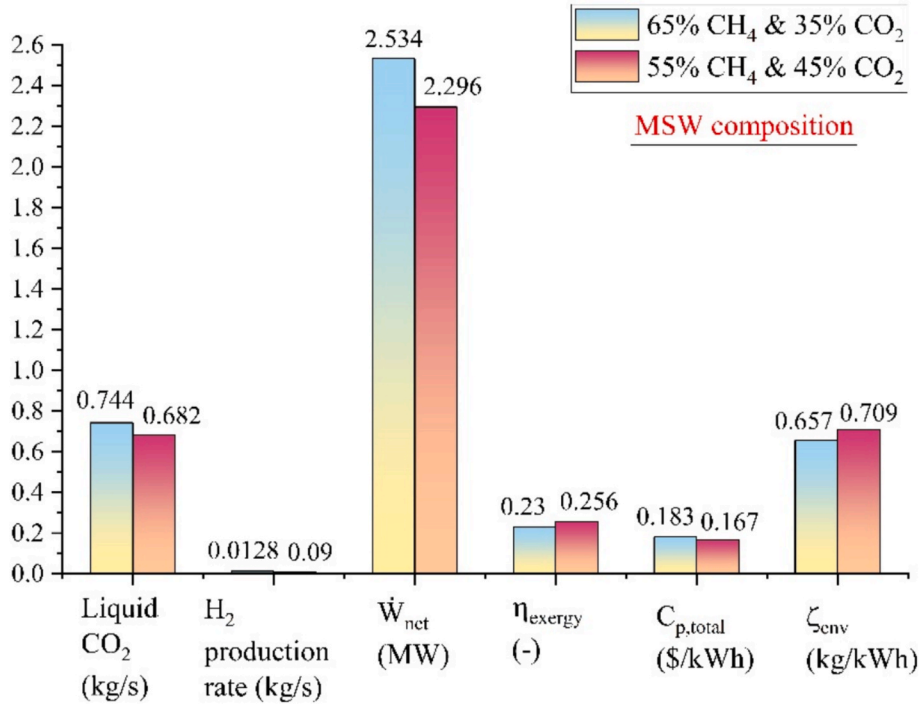

Fig. 15. The variation of the key indicators of the system versus the biogas composition.

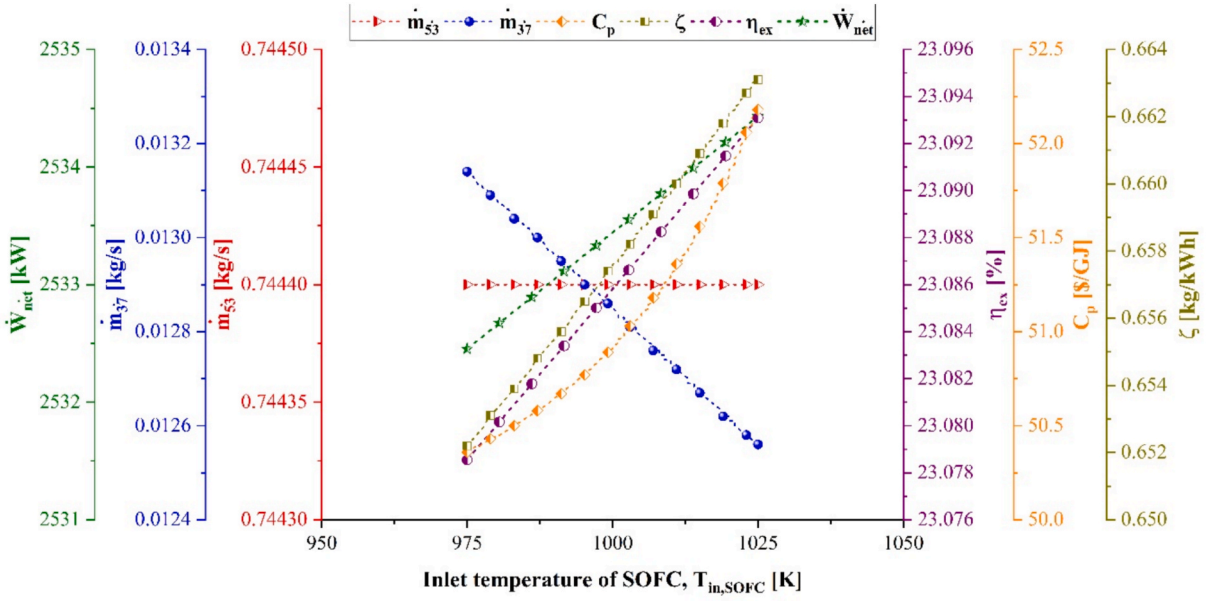

Fig. 16. The variation of the key indicators of the system versus the inlet temperature of SOFC.

current produced by the cell. Since power is the product of voltage and current, this directly enhances power output. However, this must be balanced carefully—very high fuel utilization can lead to local fuel starvation near the outlet, causing voltage drop or even anode degradation. Within safe limits, though, increasing fuel utilization improves overall fuel efficiency and electrical performance.

Conversely, the environmental index and total cost of products (Cp) decline with increasing fuel utilization. The reduction in the environmental index suggests that the system becomes more sustainable as it extracts more energy from the same fuel input, reducing emissions per unit of power generated. Meanwhile, the decrease in Cp indicates that the system's economic performance improves, as the increased energy output reduces the cost per unit of useful energy produced.

Interestingly, the amounts of captured CO_2 and hydrogen production remain unchanged, meaning that increasing UF does not affect the system's CO_2 separation or hydrogen generation. This suggests that CO_2 capture is primarily influenced by combustion processes, while hydrogen production depends on the operating conditions of the vanadium chloride cycle rather than SOFC fuel utilization.

Both layouts (a) and (b) in this figure exhibit the same general trends, but Figure (a) consistently shows better performance as explained above.

Overall, increasing the fuel utilization factor enhances system efficiency, power generation, and sustainability while lowering costs, with

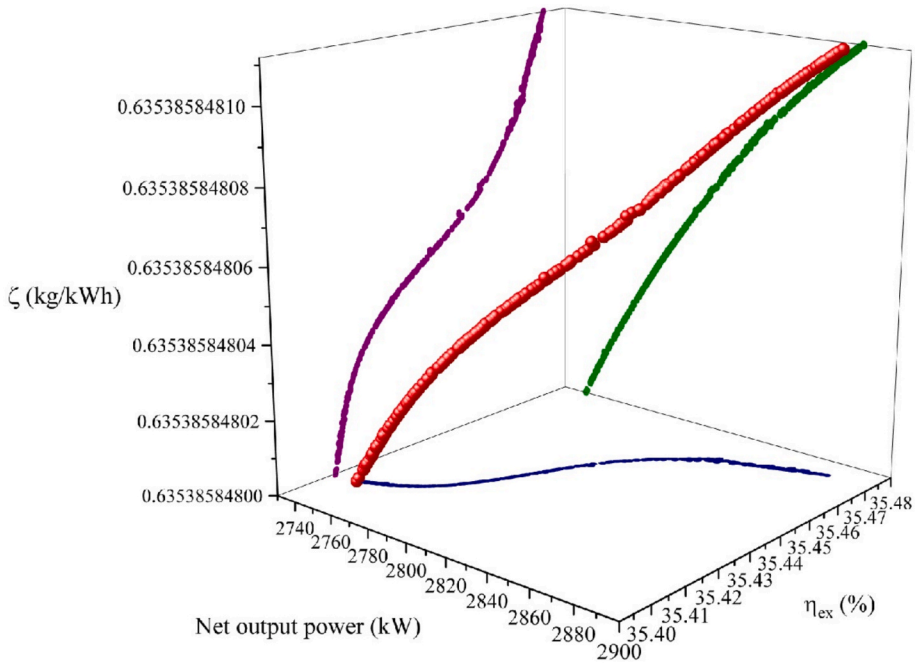

Fig. 17. The Pareto front graph for the first scenario.

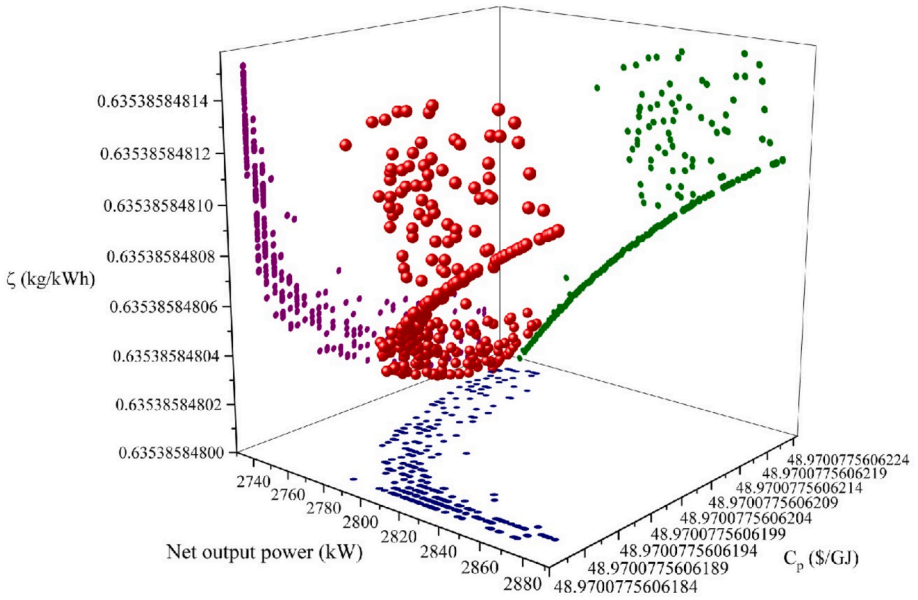

Fig. 18. The Pareto front graph for the second scenario.

the TPV-integrated system consistently demonstrating superior performance.

To investigate the sensitivity of the system to biogas composition, a parametric analysis was conducted using two different methane mole fractions: 65 % CH_4 / 35 % CO_2 and 55 % CH_4 / 45 % CO_2, representing realistic variability in the organic fraction of Municipal Solid Waste (MSW). In Fig. 15, as the methane content increases, the system shows an increase in liquid CO_2 capture, hydrogen production rate, and net output power. However, a slight reduction in exergy efficiency is observed. This occurs because a higher methane fraction increases the input exergy of the biomass (due to methane's higher lower heating value), but the net power output and recoverable exergy do not increase proportionally—particularly because a significant portion of power is consumed in the CO_2 capture and liquefaction processes. Consequently, the system becomes less effective at converting available exergy into useful work. Despite this, environmental performance (represented by the emission index, ζ) improves, showing that higher methane content favors cleaner operation, although at the expense of thermodynamic efficiency.

To examine the sensitivity of the system to changes in SOFC inlet temperature, a parametric analysis was performed over the range of 950 K to 1050 K, which reflects realistic operating conditions for solid oxide fuel cells. As shown in Fig. 16, increasing the inlet temperature leads to a slight increase in net power output and exergy efficiency, due to improved electrochemical reaction kinetics and reduced internal resistances at higher temperatures. However, this improvement is moderate because the majority of the system's power is still generated by the gas turbine and closed Brayton cycle, which are less directly influenced

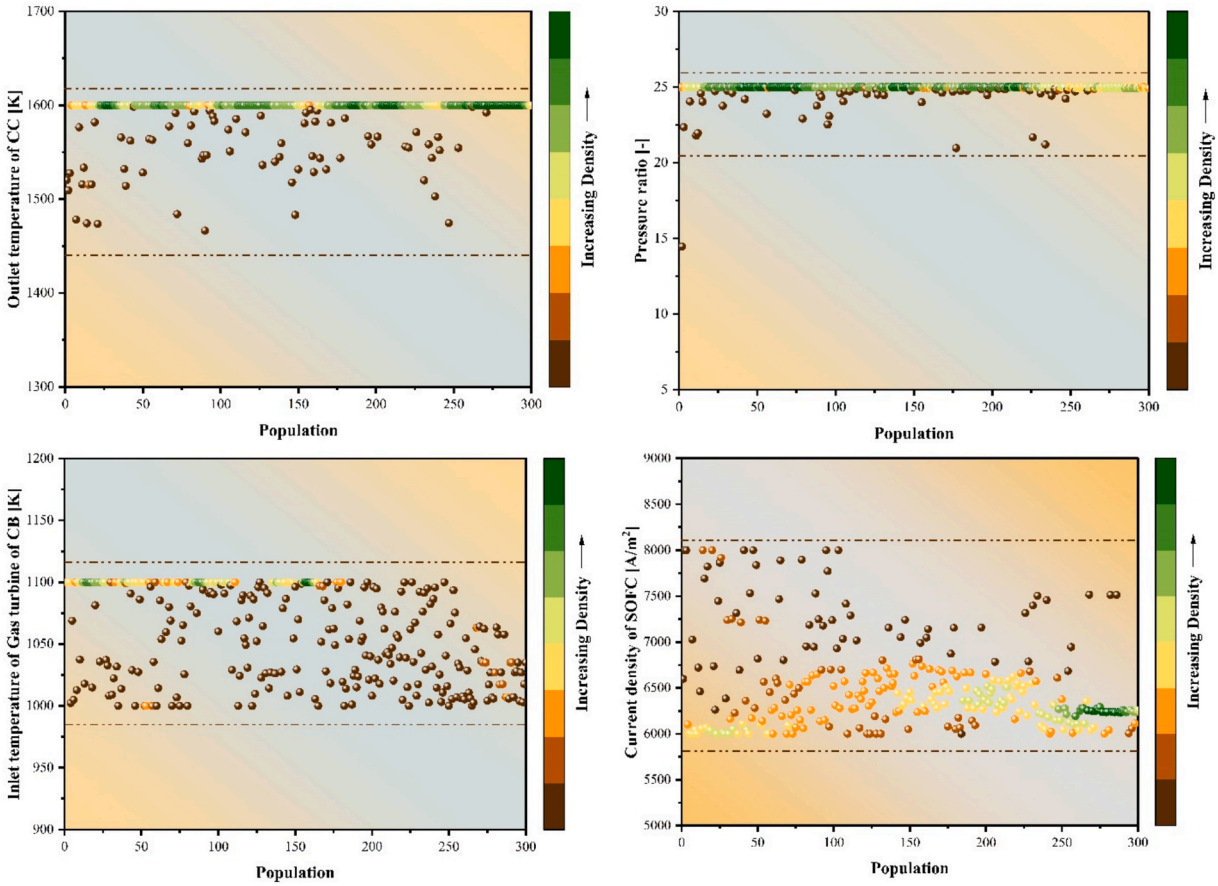

Fig. 19. Scatter distribution for the decision variables for first scenario.

by SOFC inlet conditions.

Interestingly, the hydrogen production rate ($\dot{m}_{37}$) decreases with higher inlet temperatures. This behavior is attributed to reduced excess heat available for the vanadium chloride hydrogen production cycle, since more of the thermal energy is used internally within the SOFC and Brayton cycles. The liquefied CO_2 rate ($\dot{m}_{53}$) remains nearly constant, indicating that CO_2 separation performance is not significantly affected in this temperature range. Meanwhile, Cp,total increases slightly with temperature, likely due to rising thermal losses and cost of maintaining structural integrity at higher temperatures. The environmental impact indicator (ζ) improves moderately, reflecting reduced emissions per unit of useful output as efficiency improves.

5.3. Optimization

This section outlines the findings derived from the multi-objective optimization conducted through the Multi-Objective Grey Wolf Optimizer (MOGWO) approach. Increased focus is directed toward critical decision-making factors including the output temperature of the combustion chamber (T_{10}), the pressure ratio of compressors and turbines (Pr), the inlet turbine temperature (T_{38}), and the current density of SOFC (j). The optimization is carried out under two distinct scenarios, with Figs. 17 and 18 showcasing the Pareto frontier produced by the MOGWO method. The LINMAP technique is subsequently employed to determine the most effective solution from this frontier.

Fig. 17 illustrates the optimization outcomes for the initial scenario, revealing an exergy efficiency of 35.44 %, a net output power of 2798 kW, and an emission index of 0.6353 kg/kWh as the most suitable solution.

Fig. 18 displays the optimization results for the second scenario, where the optimal solution includes 0.63 kg/kWh emission index, a net output power of 2816 kW, and a unit exergy cost of total products at 48.97 $/GJ.

The exergy efficiency improves marginally, but the return on efficiency gain diminishes as ζ_{env} and Cp start increasing rapidly. This highlights a zone of diminishing returns, where further efficiency improvement comes at higher environmental and economic costs. This suggests that even though cleaner operation is possible, achieving higher exergy efficiency results in less favorable emission outcomes, pointing to a trade-off region. These figures underline the importance of balancing thermodynamic performance with environmental and economic goals, and help stakeholders choose configurations based on specific priorities.

Scatterplots are employed to depict the limitations of the optimization approach, the convergence of individual variables, and the evaluated values. In the first scenario, depicted in Fig. 19, the ideal output temperature of the combustion chamber for the digesting unit is determined to be 1600 K, attributed to population clustering at this value. The ideal pressure ratio for compressors and turbines is 25. The ideal current density of the SOFC unit varies between 6000 and 6750 A/m^2. The ideal intake temperature of a gas turbine in a closed Brayton cycle ranges from 1000 to 1100 K, affected by clustering within this interval.

In the second scenario, as illustrated in Fig. 20, the ideal outlet temperature of the combustion chamber for the digestion unit has been determined to be 1600 K, reflecting a significant concentration of values around this point. The ideal inlet temperature for the gas turbine in a closed Brayton cycle fluctuates within the designated range of 1000–1100 K, shaped by the dynamics present within this spectrum. The ideal pressure ratio for compressors and turbines stands at 25. The ideal current density for a SOFC unit stands at 6000 A/m^2.

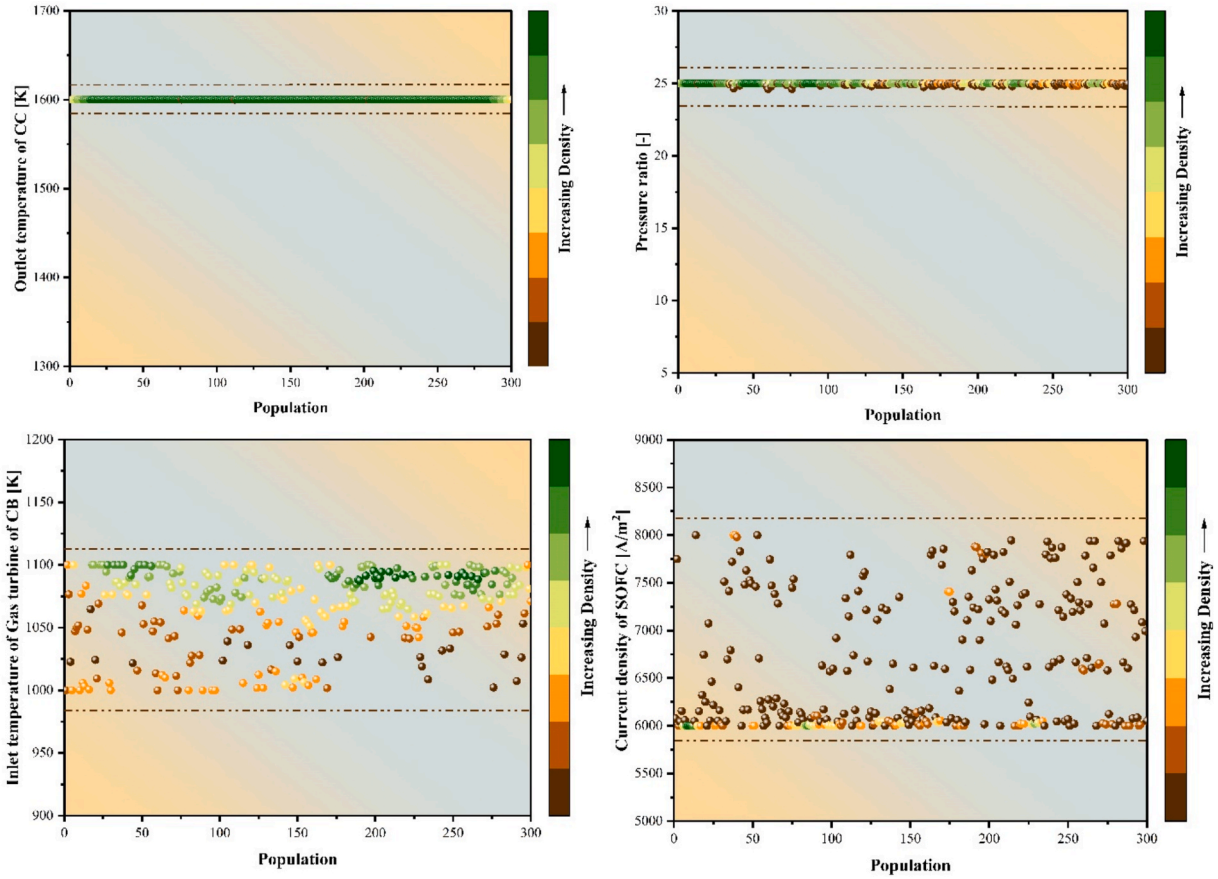

Fig. 20. Scatter distribution for the decision variables for second scenario.

6. Conclusions

This study proposed a novel multi-generation system integrating a digestion unit, SOFC, TPV unit, closed Brayton cycle, vanadium chloride hydrogen production unit, and CO_2 liquefaction unit. The system efficiently utilizes biogas and air, directing them into separate pathways for combustion and SOFC power generation. Waste heat is recovered to enhance efficiency, drive a gas turbine, and support additional processes like hydrogen production and CO_2 capture using LNG cooling. A comprehensive energy, exergy, and techno-economic analysis was conducted, along with multi-objective optimization using the Grey Wolf Optimizer (GWO) algorithm in two scenarios. The main conclusions are as follows:

- The system achieves a net power output of 2,542 kW, a second law efficiency of 25.27 %, and hydrogen production of 0.01285 kg/s, with CO_2 emissions reduced from 0.6562 kg/kWh to 0.63 kg/kWh through liquefaction.
- The NPV analysis indicates that higher electricity selling prices significantly shorten payback times, with the most favorable case of 0.12 $/kWh achieving returns in under four years for a 10-year lifespan and under seven years for a 20-year lifespan.
- The highest exergy destruction occurs in the combustion chamber (2,231 kW), followed by the vanadium chloride unit (1,125 kW) and digester (1,080 kW), while the TPV unit utilizes 585.3 kW of SOFC radiative heat loss to generate 116 kW, improving both system efficiency and economic feasibility.
- Parametric studies indicate that combustion chamber temperature has the most significant impact on system performance, as higher temperatures enhance $\dot{W}_{net}$, exergy efficiency, and hydrogen production while reducing the environmental index and CO_2 capture. Additionally, the TPV unit improves energy recovery, economic feasibility, and environmental sustainability, making it a valuable addition to the system.
- Optimization results show that in Scenario 1, the system achieves 35.44 % exergy efficiency, 2,798 kW net power, and a 0.6353 kg/kWh emission index, while in Scenario 2, it attains 2,816 kW net power, a 0.63 kg/kWh emission index, and a unit exergy cost of 48.97 $/GJ.

The proposed system demonstrates high efficiency, environmental benefits, and economic viability, making it a promising solution for sustainable multi-generation applications. In future studies, integrating SOFC for power generation could be highly beneficial due to their high electrical efficiency. However, as SOFCs release substantial waste heat, coupling them with TPV units may significantly enhance overall system efficiency. Additionally, converting system outputs such as hydrogen and captured CO_2 into synthetic fuels like methanol or SNG presents a valuable opportunity for broadening the system's utility and sustainability impact.

CRediT authorship contribution statement

Shayan Rabet: Writing – original draft, Visualization, Validation, Software, Resources, Project administration, Methodology, Investigation, Formal analysis, Data curation, Conceptualization. **Shayan Sharafi Laleh:** Writing – original draft, Visualization, Validation, Software, Resources, Project administration, Methodology, Formal analysis, Data curation, Conceptualization. **Omid Habibi:** Writing – original draft, Visualization, Validation, Software, Resources, Project administration, Methodology, Investigation, Formal analysis, Data curation, Conceptualization. **Seyed Ali Sadri Jahanshahi:** Writing – original draft,

Visualization, Validation, Software, Resources, Project administration, Methodology, Investigation, Formal analysis, Data curation, Conceptualization. **Mortaza Yari:** Writing – original draft, Visualization, Validation, Software, Resources, Project administration, Methodology, Investigation, Formal analysis, Data curation, Conceptualization. **Saeed Soltani:** Writing – original draft, Visualization, Validation, Supervision, Software, Resources, Project administration, Methodology, Investigation, Formal analysis, Data curation, Conceptualization.

Declaration of competing interest

The authors declare that they have no known competing financial interests or personal relationships that could have appeared to influence the work reported in this paper.

Appendix A. Supplementary data

Supplementary data to this article can be found online at https://doi.org/10.1016/j.fuel.2025.136581.

Data availability

The authors are unable or have chosen not to specify which data has been used.

References

[1] Wen D, Aziz M. Data-driven energy management system for flexible operation of hydrogen / ammonia-based energy hub : a deep reinforcement learning approach. Energy Convers Manag 2023;291:117323. https://doi.org/10.1016/j.enconman.2023.117323.

[2] Wen D, Aziz M. Perspective of staged hydrogen economy in Japan : a case study based on the data-driven method. Renew Sustain Energy Rev 2024;189:113907. https://doi.org/10.1016/j.rser.2023.113907.

[3] Wen D, Liu S, Ning Z, Aziz M. Techno-economic evaluation of hydrogen and ammonia as energy carriers in a multi-generation system. Energy Convers Manag 2023;277:116670. https://doi.org/10.1016/j.enconman.2023.116670.

[4] Silva-mosqueda DM, Elizalde-blancas F, Pumiglia D, Santoni F, Boigues-muñoz C, Mcphail SJ. Intermediate temperature solid oxide fuel cell under internal reforming : critical operating conditions , associated problems and their impact on the performanc. Appl Energy 2019;235:625–40. https://doi.org/10.1016/j.apenergy.2018.10.117.

[5] Liao T, Cai L, Zhao Y, Chen J. Efficiently exploiting the waste heat in solid oxide fuel cell by means of thermophotovoltaic cell. J Power Sources 2016;306:666–73. https://doi.org/10.1016/j.jpowsour.2015.12.080.

[6] Irfan HM, Yang C, Wu W, Lin B, Shiau J. Environmental and techno-economic analyses of oxygen blast furnace systems integrated with carbon capture and utilization strategy. Fuel Process Technol 2025;274:108238. https://doi.org/10.1016/j.fuproc.2025.108238.

[7] Calise F, Cappiello FL, Cimmino L, Dentice d'Accadia M, Vicidomini M. A solar-assisted liquefied biomethane production by anaerobic digestion: Dynamic simulations for harbors. Renew Sustain Energy Rev 2024;189. https://doi.org/10.1016/j.rser.2023.114066.

[8] Zare V, Hasanzadeh M. Energy and exergy analysis of a closed Brayton cycle-based combined cycle for solar power tower plants. Energy Convers Manag 2016;128:227–37. https://doi.org/10.1016/j.enconman.2016.09.080.

[9] Hai T, Alazzawi AK, Ju Y, Wang D, Wang S. Integration of vanadium-chlorine thermochemical cycle with a nano-particle aided solar power tower for power and hydrogen cogeneration. Int J Hydrogen Energy 2024;52:580–93. https://doi.org/10.1016/j.ijhydene.2023.05.005.

[10] Safari F, Dincer I. Assessment and multi-objective optimization of a vanadium-chlorine thermochemical cycle integrated with algal biomass gasification for hydrogen and power production. Energy Convers Manag 2022;253:115132. https://doi.org/10.1016/j.enconman.2021.115132.

[11] Balta MT, Dincer I, Hepbasli A. Comparative assessment of various chlorine family thermochemical cycles for hydrogen production. Int J Hydrogen Energy 2016;41:7802–13. https://doi.org/10.1016/j.ijhydene.2015.12.222.

[12] Ding X, Zhou Y, Zheng N, Wang Y, Yang M, Duan L. Energy , exergy , and economic analyses of a novel liquid air energy storage system with cooling , heating , power , hot water , and hydrogen cogene. Energy Convers Manag 2024;305:118262. https://doi.org/10.1016/j.enconman.2024.118262.

[13] Ding X, Zhou Y, Zheng N, Desideri U, Duan L. Emergy analysis and comprehensive sustainability investigation of a solar-aided liquid air energy storage system based on life cycle assessment. Appl Energy 2024;365:123249. https://doi.org/10.1016/j.apenergy.2024.123249.

[14] Zhang X, Liu W, Pan J, Zhao B, Yi Z, He X, et al. Comprehensive performance assessment of a novel biomass-based CCHP system integrated with SOFC and HT-PEMFC. Energy 2024;295:131112. https://doi.org/10.1016/j.energy.2024.131112.

[15] Saberi Mehr A, Ilkhani M, Sabernia S, Nooshmand S, Ebrahimpour A, Heydari B. Thermodynamic modelling and optimisation of a green hydrogen-blended syngas-fueled integrated PV-SOFC system. Appl Therm Eng 2024;236:121506. https://doi.org/10.1016/j.applthermaleng.2023.121506.

[16] Yang P, Zhang Y, Yang C, Chen J, Liu Z, Deng C, et al. Thermodynamic performance comparison of a SOFC system integrated with steam reforming and dry reforming by utilizing different fuels. Energy Convers Manag 2024;300:117981. https://doi.org/10.1016/j.enconman.2023.117981.

[17] Wen D, Aziz M. Techno-economic analyses of power-to-ammonia-to-power and biomass-to-ammonia-to-power pathways for carbon neutrality scenario advancement of cost engineering. Appl Energy 2022;319:119272. https://doi.org/10.1016/j.apenergy.2022.119272.

[18] Ma C, Yu H, Monticone G, Ma S, Van J, Wang L. Techno-economic evaluation of biogas-fed SOFC systems with novel biogas purification and carbon capture technologies. Renew Energy 2024;235:121302. https://doi.org/10.1016/j.renene.2024.121302.

[19] Li Z, Zhang X, He X, Wu G, Tian S, Zhang D. Comparative analysis of thermal economy of two SOFC-GT-ST triple hybrid power systems with carbon capture and LNG cold energy utilization. Energy Convers Manag 2022;256:115385. https://doi.org/10.1016/j.enconman.2022.115385.

[20] Shan S, Chen B, Tian J, Zhou Z, Zhang Y. Improving the performance of steam power cycle through thermo-photovoltaic device: a novel combined system and thermodynamic analysis. Energy Convers Manag 2022;269:116139. https://doi.org/10.1016/j.enconman.2022.116139.

[21] Yang Z, Xu H, Chen B, Tan P, Zhang H, Ni M. Numerical modeling of a cogeneration system based on a direct carbon solid oxide fuel cell and a thermophotovoltaic cell. Energy Convers Manag 2018;171:279–86. https://doi.org/10.1016/j.enconman.2018.05.100.

[22] Yari M, Mehr AS, Mahmoudi SMS, Santarelli M. A comparative study of two SOFC based cogeneration systems fed by municipal solid waste by means of either the gasifier or digester. Energy 2016;114:586–602. https://doi.org/10.1016/j.energy.2016.08.035.

[23] Fakhari I, Behzadi A, Gholamian E, Ahmadi P, Arabkoohsar A. Design and tri-objective optimization of a hybrid efficient energy system for tri-generation, based on PEM fuel cell and MED using syngas as a fuel. J Clean Prod 2021;290. https://doi.org/10.1016/j.jclepro.2020.125205.

[24] Dou Z, Zou Y, Mohebbi A. Design and multi-aspect analysis of a geothermal and biomass dual-source power, cooling, heating, and hybrid freshwater production sys. Energy 2024;293:130532. https://doi.org/10.1016/j.energy.2024.130532.

[25] Baccioli A, Ferrari L, Vizza F, Desideri U. Potential energy recovery by integrating an ORC in a biogas plant. Appl Energy 2019;256. https://doi.org/10.1016/j.apenergy.2019.113960.

[26] Sharafi Laleh S, Safarpour A, Shahbazi Shahrak A, Fatemi Alavi SH, Soltani S. Thermodynamic and exergoeconomic analyses of a novel biomass-fired combined cycle with solar energy and hydrogen and freshwater production in sports arenas. Int J Hydrogen Energy 2024;59:1507–17. https://doi.org/10.1016/j.ijhydene.2024.02.146.

[27] Bejan A, Tsatsaronis G, Moran MJ. Thermal design and optimization. John Wiley & Sons; 1995.

[28] Bejan A. Advanced engineering thermodynamics. John Wiley & Sons; 2016.

[29] Zhang L, Sobhani B. Comprehensive economic analysis and multi-objective optimization of an integrated power and freshwater generation cycle based on flash-binary geothermal and gas turbine cycles. J Clean Prod 2022;364. https://doi.org/10.1016/j.jclepro.2022.132644.

[30] Zhang L, Sobhani B. Comprehensive economic analysis and multi-objective optimization of an integrated power and freshwater generation cycle based on flash-binary geothermal and gas turbine cycles. J Clean Prod 2022;364:132644. https://doi.org/10.1016/j.jclepro.2022.132644.

[31] Gao Z, Miao J, Zhao J, Mesri M. Comprehensive economic analysis and multi-objective optimization of an integrated gasification power generation cycle. Process Saf Environ Prot 2021;155:61–79. https://doi.org/10.1016/j.psep.2021.09.007.

[32] Steven A. Thermochemical hydrogen produced from a vanadium decomposition cycle. US Pat No 8,287,838 B2 Washington. DC US Pat Trademark Off 2012;2.

[33] The Exergoecology Portal n.d. http://www.exergoecology.com/excalc.

[34] Sadeghi M, Chitsaz A, Mahmoudi SMS, Rosen MA. Thermoeconomic optimization using an evolutionary algorithm of a trigeneration system driven by a solid oxide fuel cell. Energy 2015;89:191–204. https://doi.org/10.1016/j.energy.2015.07.067.

[35] Massardo A, Lubelli F. Internal reforming solid oxide fuel cell-gas turbine combined cycles (IRSOFC-GT): Part A—cell model and cycle thermodynamic analysis. J Eng Gas Turbines Power-Transactions Asme - J ENG GAS TURB POWER-T ASME 2000;122:27–35. https://doi.org/10.1115/1.483187.

[36] Bossel UG, Dubal L. Facts and figures, an International Energy Agency SOFC task report 1992.

[37] Kim J, Virkar AV, Fung K, Mehta K, Singhal SC. Polarization effects in intermediate temperature, anode-supported solid oxide fuel cells. J Electrochem Soc 1999;146:69. https://doi.org/10.1149/1.1391566.

[38] Chan SH, Low CF, Ding OL. Energy and exergy analysis of simple solid-oxide fuel-cell power systems. J Power Sources 2002;103. https://doi.org/10.1016/S0378-7753(01)00842-4.

[39] Petruzzi L, Cocchi S, Fineschi F. A global thermo-electrochemical model for SOFC systems design and engineering. J Power Sources 2003;118:96–107. https://doi.org/10.1016/S0378-7753(03)00067-3.

[40] Zarabi S, Imran M, Lund PD. A review on solid oxide fuel cell durability : latest progress, mechanisms, and study too. Renew Sustain Energy Rev 2022;161:112339. https://doi.org/10.1016/j.rser.2022.112339.
[41] Chouhan K, Sinha S, Kumar S, Kumar S. Utilization of biogas from different substrates for SOFC feed via steam reforming: thermodynamic and exergy analyses. J Environ Chem Eng 2019;7:103018. https://doi.org/10.1016/j.jece.2019.103018.
[42] Liao T, He Q, Xu Q, Dai Y, Cheng C, Ni M. Harvesting waste heat produced in solid oxide fuel cell using near-field thermophotovoltaic cell. J Power Sources 2020;452. https://doi.org/10.1016/j.jpowsour.2020.227831.
[43] Dong Q, Cai L, Liao T, Zhou Y, Chen J. An efficient coupling system using a thermophotovoltaic cell to harvest the waste heat from a reforming solid oxide fuel cell. Int J Hydrogen Energy 2017;42:17221–8. https://doi.org/10.1016/j.ijhydene.2017.05.201.
[44] Ferrari C, Melino F, Bosi M. The critical role of emitter size in thermo-photovoltaic generators. Sol Energy Mater Sol Cells 2013;113:20–5. https://doi.org/10.1016/j.solmat.2013.01.031.
[45] Shan S, Zhou Z, Wang Z, Cen K. New oxy-fuel cascade thermo-photovoltaic energy conversion system: effect of cascade design and oxygen ratio. Energy Convers Manag 2019;196:1208–21. https://doi.org/10.1016/j.enconman.2019.06.080.
[46] Hamrang F, Shokri A, Seyed Mahmoudi SM, Ehghaghi B, Rosen MA. Performance analysis of a new electricity and freshwater production system based on an integrated gasification combined cycle and multi-effect desalination. Sustain 2020;12:1–29. https://doi.org/10.3390/su12197996.
[47] Gholamian E, Mehr AS, Yari M, Carton JG. Dynamic simulation and techno-economic assessment of hydrogen utilization in dual fuel (Hydrogen/biogas) micro gas turbine systems for a wastewater treatment plant. Process Saf Environ Prot 2023;169:220–37. https://doi.org/10.1016/j.psep.2022.10.045.
[48] Verma S, Buznitsky K, Henry A. Thermophotovoltaic performance metrics and techno-economics: efficiency vs. power density. Appl Energy 2025;384. https://doi.org/10.1016/j.apenergy.2025.125479.
[49] Liu Y, Han J, You H. Exergoeconomic analysis and multi-objective optimization of a CCHP system based on LNG cold energy utilization and flue gas waste heat recovery with CO2 capture. Energy 2020;190. https://doi.org/10.1016/j.energy.2019.116201.
[50] Ghasemzadeh N, Javaherian A, Yari M, Nami H. Energy Conversion and Management : X thermodynamics modelling and optimisation of a biogas fueled decentralised poly-generation system using machine learning techniques. Energy Convers Manag X 2023;20:100470. https://doi.org/10.1016/j.ecmx.2023.100470.
[51] Deng J, Tang Y, Tang J, Liu H, Chen W, Sun Z, et al. From sewage sludge to hydrogen: life cycle techno-environment-economic assessment of combined system with supercritical water gasification, organic Rankine cycle and carbon capture and storage. Energy Convers Manag 2025;323. https://doi.org/10.1016/j.enconman.2024.119221.
[52] Cell price of LNG 2025. https://www.reuters.com/business/energy/us-natural-gas-prices-climb-2-record-flows-lng-export-plants-2025-03-03/?utm_source=chatgpt.com.
[53] Renewable I, Agency E. Renewable Generation Costs in 2023 2023.
[54] Ayres RU, Ayres LW, Martinas K. Eco-thermodynamics: exergy and life cycle analysis 1996.
[55] Mirjalili S, Mohammad S, Lewis A. Grey wolf optimizer. Adv Eng Softw 2014;69:46–61. https://doi.org/10.1016/j.advengsoft.2013.12.007.
[56] Mahmoudi SMS, Salehi S, Yari M. Three-objective optimization of a novel triple-effect absorption heat transformer combined with a water desalination system. Energy Convers Manag 2017;138:131–47. https://doi.org/10.1016/j.enconman.2017.01.057.
[57] Tao G, Armstrong T, Virkar A. Intermediate temperature solid oxide fuel cell (IT-SOFC) research and development activities at MSRI. Provo, UT: Ninet. Annu. ACERC&ICES Conf; 2005.
[58] Höber M, Königshofer B, Schröttner H, Fitzek H, Menzler NH, Hochenauer C, et al. Experimental identification of the impact of direct internal and external methane reforming on SOFC by detailed online monitoring and supporting measurements. J Power Sources 2023;581:233449. https://doi.org/10.1016/j.jpowsour.2023.233449.
[59] Javaherian A, Yari M, Gholamian E, Carton JG, Mehr AS. Proposal and comprehensive analysis of power and green hydrogen production using a novel integration of flame-assisted fuel cell system and vanadium-chlorine cycle: an application of multi-objective optimization. Energy Convers Manag 2023;277. https://doi.org/10.1016/j.enconman.2023.116659.
[60] Laleh SS, Rezaei Mousavi HS, Rabet S, Nojavan F, Yari M, Soltani S. Solar thermal assisted proton exchange membrane electrolyzer and solid oxide fuel cell system based on biomass gasification for green power and hydrogen production: multi-objective optimization and exergoeconomic analysis. Energy Convers Manag 2025;337. https://doi.org/10.1016/j.enconman.2025.119900.